Chemical Science

ROYAL SOCIETY OF CHEMISTRY

REVIEW

View Article Online
View Journal | View Issue

Cite this: *Chem. Sci.*, 2024, **15**, 15983

2D compounds with heterolayered architecture for infrared photodetectors

Hao Gu, Tianshuo Zhang, Yunluo Wang, Tianrui Zhou and Haijie Chen *

Compounds with heterolayered architecture, as a family of two-dimensional (2D) materials, are composed of alternating positive and negative layers. Their physical properties are determined not only by the charged constituents, but also by the interaction between the two layers. This kind of material has been widely used for superconductivity, thermoelectricity, energy storage, *etc.* In recent years, heterolayered compounds have been found as an encouraging choice for infrared photodetectors with high sensitivity, fast response, and remarkable reliability. In this review, we summarize the research progress of heterolayered materials for infrared photodetectors. A simple development history of the materials with three-dimensional (3D) or 2D structures, which are suitable for infrared photodetectors, is introduced firstly. Then, we compare the differences between van der Waals layered 2D materials and heterolayered 2D cousins and explain the advantages of heterolayered 2D compounds. Finally, we present our perspective on the future direction of heterolayered 2D materials as an emerging class of materials for infrared photodetectors.

Received 25th May 2024
Accepted 7th September 2024

DOI: 10.1039/d4sc03428g

rsc.li/chemical-science

1. Introduction

Infrared detectors, which are used to detect and measure infrared radiation, have been widely used for military, security, environmental monitoring and industrial applications.[1–4] They can be divided into infrared thermal detectors and infrared photodetectors. Infrared thermal detectors are based on thermocouples, which are composed of two different semiconductors or conductors. Under infrared light irradiation, these two kinds of materials have different temperatures, which leads to the movement of electrons inside the thermocouple and the creation of an electric potential.[5,6] For infrared photodetectors, the working mechanism is to convert the optical signals to the electrical ones based on the photovoltaic effect or photoconductive effect.[7,8] Compared with infrared thermal detectors, infrared photodetectors have the advantages of higher sensitivity, faster response, broader wavelength range response and higher reliability.[9] For infrared photodetectors, the core lies in the properties of the materials which basically have high sensitivity to infrared light.

Two-dimensional (2D) materials have been identified as an intriguing large family for infrared photodetectors, and the discovery of single-layer graphene in 2004 sparked interest in the application of 2D materials for infrared photodetectors.[10] Compared with 3D materials, 2D materials generally exhibit higher photoelectric conversion efficiency and sensitivity, which allows 2D materials to respond more accurately and quickly when being used to detect infrared light signals. Due to the unique layered structure of 2D materials, electrons and holes move quickly in the 2D plane, and infrared photodetectors based on 2D materials usually have shorter response times and are able to detect changes in infrared light signals more quickly.[11,12] Moreover, 2D materials often have a broad spectral response range, and some 2D materials even perform well in the ultraviolet (UV), visible (VIS), and terahertz (THz) bands, making them suitable for a broader range of applications. Black phosphorus has similar properties to graphene, with a broad absorption spectrum and high carrier mobility.[13,14] In recent years, transition metal chalcogenides, such as MoS_2 and WS_2, have shown potential for photodetection due to their high light absorption coefficients and tunable bandgaps.[15,16] However, one coin always has two sides. Different from their 3D counterparts, 2D materials also have some problems, such as high anisotropy and complex production processes.[17–20]

Heterolayered materials refer to 2D materials that are bonded by ionic or covalent interactions between the constituents.[21] The crystal structures of these kinds of 2D compounds are composed of alternating positive and negative layers. Multiple choices of the positive or negative layers contribute to the large quantity of heterolayered compounds. Usually, either a positive or negative constituent determines the physical properties of the heterolayered compounds, in which the other layer stabilizes the whole structure. Besides, the bonding between the two layers also contributes to the properties of the compounds. Hereby, the unique heterolayered structures endow them with the properties of 3D bulk materials and the

State Key Laboratory for Modification of Chemical Fibers and Polymer Materials, Institute of Functional Materials, College of Materials Science and Engineering, Donghua University, Shanghai, 201620, China. E-mail: haijie.chen@dhu.edu.cn

superiority of 2D geometric structures, marking them particularly suitable for the field of infrared photodetection. Up to now, several heterolayered 2D compounds have been reported for infrared photodetectors. The responsivity of the Bi_2O_2Te-based infrared detector is up to 10^4 A W^{-1} and the detectivity is up to 10^{14} jones, showing excellent infrared detection performance.[22] Photodetectors based on $EuMTe_3$ (M = Bi, Sb) can achieve a response of >1 A W^{-1} from the UV band to the THz band.[23,24] The photodetector, which is based on the MXene (Mo_2CT_x) material, exhibits a responsivity of 9 A W^{-1} and a detectivity of 5 $\times$ 10^{11} jones under 660 nm laser irradiation. It shows a good photoresponse in the wavelength range of 325 nm to 1064 nm.[25] So far, research on heterolayered materials is still in its infancy. More interest deserves to be devoted to this kind of compound.

Up to now, there have been several decent reviews about 2D materials for infrared photodetectors.[26–29] However, there has been no special review about the heterolayered 2D compounds. As an emerging family of materials with superior performance for infrared photodetectors, their progress needs to be summarized. Here, we reviewed the reports of heterolayered materials used for infrared detectors. The crystal structures and properties of the infrared detectors are discussed in detail. Finally, we forecast the fields where the infrared detectors could be used.

2. Parameters of photodetectors

The diverse application scenarios are based on the parameters of photodetectors. The following parameters are generally used to evaluate the performance of a photodetector: responsivity, external quantum efficiency, noise equivalent power, detectivity, and response time. This chapter will introduce the parameters of photodetectors and discuss their effects on device performance.

2.1 Responsivity

The responsivity (R) is defined as the formula (1) and (2) which refers to the ratio of the output photocurrent ($I_{\text{photocurrent}}$) or output voltage ($V_{\text{photovoltage}}$) to the incident light power (p) under illumination. It indicates the ability of the detector to receive signals. The magnitude of responsivity directly affects the sensitivity and accuracy of photodetectors. The higher the responsivity, the more sensitive the photodetectors to the light signal. There are many factors that affect the responsivity of photodetectors. One of the important factors is the photoconductive gain (G). The gain can be alternatively expressed as the number of photogenerated electron–hole pairs collected by contact to generate a net photocurrent (I_{ph}) divided by the number of photoexcited electron–hole pairs. Therefore, the responsivity can be improved by higher I_{ph} generated by the increased gain.[26]

$$R = \frac{I_{\text{photocurrent}}}{P} \tag{1}$$

$$R = \frac{V_{\text{photovoltage}}}{P} \tag{2}$$

2.2 External quantum efficiency

External quantum efficiency (EQE) refers to the efficiency of converting photons into electrons when photodetectors receive optical signals. Generally speaking, it is the efficiency of photoelectric conversion. The EQE directly affects the sensitivity and signal-to-noise ratio of the detectors. The calculation formula of EQE is:

$$\text{EQE} = \frac{hc}{q\lambda}R \tag{3}$$

where λ is the wavelength of the incident light, q is the electron charge, h is the Planck constant, c is the speed of light, and R is the responsivity. The EQE is usually tested in the visible light band or infrared band, and its numerical range is generally between 0 and 1.[30–32] The higher the EQE, the higher the conversion efficiency of the detectors to the optical signal.

Improving the EQE of photodetectors is one of the important ways to improve their performance. In order to improve the EQE, we can start from the following aspects: (1) optimize the structure design of the detectors, including the material selection and thickness design of the photodetector conversion layer, so as to improve the interaction efficiency between photons and electrons; (2) optimize the preparation process of the detectors, improve the purity and uniformity of the material, and reduce the influence of defects and impurities on the photodetector conversion; (3) optimize the working environment of the detectors to ensure the stable input of the optical signal, reduce the noise interference and improve the signal-to-noise ratio. In short, the EQE, as an important performance index of photodetectors, directly affects the sensitivity and signal-to-noise ratio of the detectors. By optimizing the structural design, preparation process and working environment of the detectors, the EQE of the photodetectors can be improved, thereby improving their performance.[33–35]

2.3 Noise equivalent power

Noise equivalent power (NEP) refers to the influence of noise generated by various reasons in the infrared detection system. This kind of noise will reduce the signal-to-noise ratio of the system, thus affecting the detection performance of the system.[36] The NEP directly affects the sensitivity and resolution of the system, so it has an important influence on the performance of the infrared detection system. Therefore, the noise equivalent power characterizes the minimum optical signal power that the detector can distinguish in noise. The definition is shown in formula (4).

$$\text{NEP} = \frac{i_{\text{n}}}{R} \tag{4}$$

where i_{n} is the noise current corresponding to different powers, and R is the response rate.

In the infrared detection system, the noise equivalent power mainly comes from two aspects: (1) the thermal noise of the detector itself and (2) the interference noise of the external environment. The thermal noise of the detector itself is caused by the heat generated by the detector during operation, and this

noise will increase with the increase of the detector temperature. The interference noise of the external environment is caused by electromagnetic interference, optical interference, and other factors in the surrounding environment, which will have a great impact on the detection performance of the system. By taking effective measures to reduce the influence of NEP, the detection performance and reliability of the infrared detection system can be improved, so as to meet the needs of various application fields better.[37–39]

2.4 Detectivity

The specific detectivity is also a performance index to measure the detector's ability to detect the minimum optical signal, which is defined as the reciprocal of the noise equivalent power. In order to compare the performance of different detectors in practical use, the specific detectivity is normalized, and the definition is shown in (5).

$$D^* = \frac{\sqrt{A\Delta f}}{\mathrm{NEP}} = D\sqrt{A\Delta f} \quad (5)$$

where A is the effective light-receiving area of the device, and Δf is the measurement bandwidth. At the same time, the main noise source of the photodetector is the shot noise from the dark current. Detectivity will be affected by the signal-to-noise ratio of the detector. The signal-to-noise ratio refers to the ratio of the detector between the signal and the noise. The higher the signal-to-noise ratio, the stronger the detector's ability to identify the target, and the higher the detection rate. In infrared photodetectors, the improvement of the signal-to-noise ratio can be achieved by optimizing the circuit design of the detector and reducing the thermal noise of the detector.[26]

2.5 Response time

The response time (τ) is the time interval between the photodetectors being stimulated by the optical signal and the output electrical signal. The response time is defined as the time occupied by 10% to 90% of the net photocurrent. The response speed of the detector when the signal changes is characterized. The response time is affected by many factors, such as carrier lifetime, bias voltage, and self-defect. The response time mainly depends on the lifetime of photogenerated carriers, so there is a trade-off between responsivity and response time. When the increase of carrier lifetime leads to the increase of photoconductive gain, the responsivity of the device can be improved. However, the response time of the device will increase accordingly.[40]

3. Mechanism of the photodetectors

There are many physical mechanisms for photodetectors to convert the absorbed optical signal into electrical ones. In this chapter, we focus on two mechanisms of photocurrent generation. The first is the excitation of free carriers caused by the optical effect, including the photovoltaic effect and photoconductivity effect. The second is the thermal effect, including the photothermoelectric effect and bolometric effect.[41]

3.1 Photovoltaic effect

The photovoltaic effect refers to the absorption of photons by the sample to generate photo-generated carriers when light irradiates the p–n junction. The built-in electric field separates the electrons in the p region from the holes in the n region, and the electrons and holes are stacked on both sides to produce a photoelectric field opposite to the built-in electric field (Fig. 1a).[42]

3.2 Photoconductive effect

When the incident photon energy absorbed by the semiconductor material is greater than or equal to the band gap energy, electron–hole pairs will be generated, resulting in an increase in carrier concentration. The applied voltage will cause the electron–hole pair to move in the opposite direction and generate photocurrent (Fig. 1b). This phenomenon is called the photoconductive effect. Without light illumination, an external voltage is applied to drive a limited number of free carriers to generate dark current (I_{dark}). Under illumination, the applied voltage drives the electron–hole pairs generated by the absorbed photon to produce a current ($I_{\mathrm{illumination}}$) which is larger than the dark current. The photocurrent (I_{ph}) can be expressed as $I_{\mathrm{ph}} = I_{\mathrm{illumination}} - I_{\mathrm{dark}}$, which can reflect the increase of conductivity of the same semiconductor under different conditions.[29]

3.3 Photothermoelectric effect

The photothermoelectric effect involves photon absorption, heat conduction, and thermoelectric conversion. First of all, when the photon is irradiated to the surface of the material, the material absorbs the energy of the photon, and the electrons inside the material are excited to the high energy level. These high-level electrons will move inside the material and generate heat energy. Secondly, heat conduction is an important part of the photothermoelectric effect. As the surface temperature of the material increases, thermal energy will spread to the interior of the material through heat conduction. Finally, thermoelectric conversion is a key step in the photothermoelectric effect.[41,43] When the surface temperature of the material increases, the temperature gradient inside the material causes electrons to move in the material (Fig. 1c). According to the principle of the thermoelectric effect, the temperature gradient will cause the drift and diffusion of electrons, resulting in uneven charge distribution and eventually forming a potential difference. An external circuit can capture this potential difference to generate electrical signals.[44–46]

3.4 Bolometric effect

When the incident photon generates heat, the conductance of the thermistor material changes (Fig. 1d). The photocurrent dominated by the radiative thermal effect increases linearly with the bias voltage. Unlike the photothermal effect, the photocurrent generated by the radiation thermal effect requires an external electric field.[26]

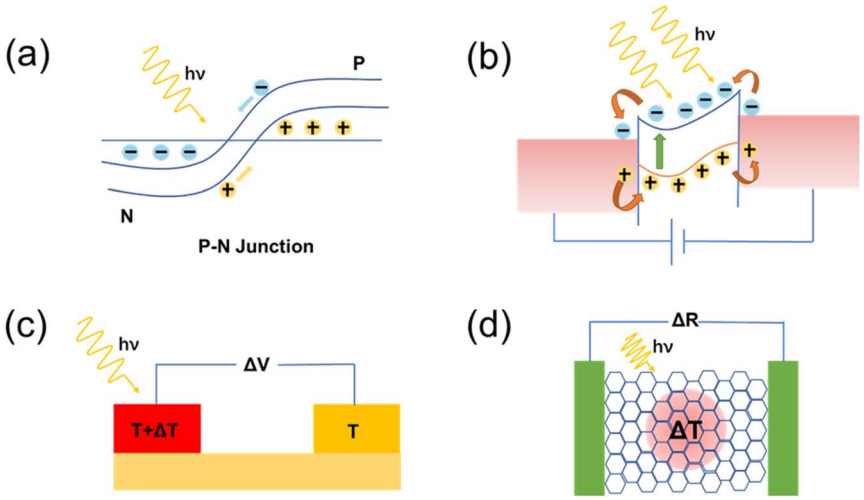

Fig. 1 The diagrams of the mechanisms for (a) the photovoltaic effect, (b) the photoconductive effect, (c) the photothermoelectric effect, and (d) the bolometric effect.

4. Development of materials for infrared photodetectors

Since Theodore W. Case prepared the first Tl_2S infrared photodetector in 1917,[47] many materials have been explored for infrared photodetectors (Fig. 2). Among them, several materials have been commercialized, such as silicon, HgCdTe, and InGaAs.[48–50] The materials suitable for infrared photodetection basically require a narrow band gap (0–1.6 eV), high carrier mobility (>10^2 cm^2 V^{-1} s^{-1}), fast response time (<10^{-6} s) and so on (Fig. 3).[5,51]

4.1 3D compounds

4.1.1 Silicon. Silicon is widely used in the field of infrared photodetection. The abundant silicon resources ensure the large-scale production of silicon and relatively low production costs. Silicon forms a diamond cubic crystal structure with a lattice spacing of 5.42 Å, which corresponds to a face-centered cubic Bravais lattice with a unit cell number containing 8 atoms at the vector position.[52] Silicon has high carrier mobility, where the carrier mobility of electrons and holes is 1350 cm^2 V^{-1} s^{-1} and 480 cm^2 V^{-1} s^{-1}, respectively.[53] At 300 K, the carrier concentration of silicon is 1.08×10^{10} cm^{-3}.[54] Silicon provides an excellent platform for the implementation of

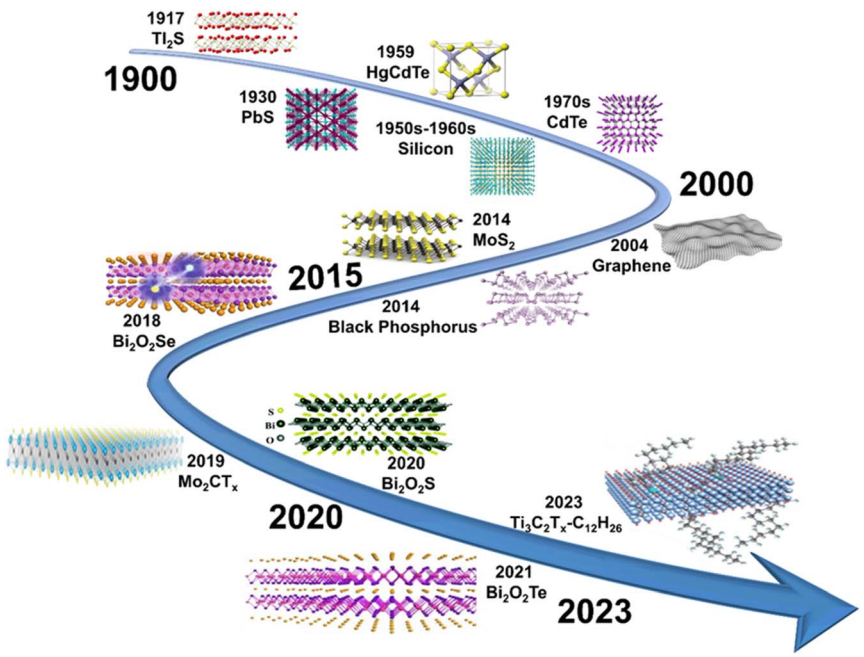

Fig. 2 Timelines of the compounds developed for infrared photodetectors.

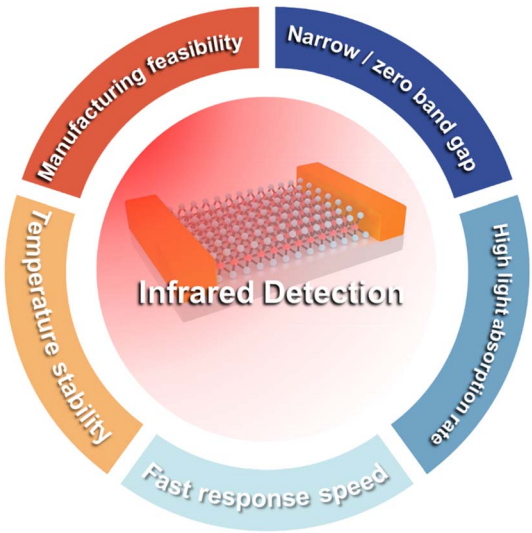

Fig. 3 Requirements of the basic properties of materials that could potentially be used for infrared photodetectors.

microelectronics-based photodetector readout circuits.[43] These merits make silicon promising for application in high-performance infrared photodetectors. Due to the inherent band gap energy of silicon (1.12 eV), the detectable spectral range is limited to wavelengths below 1100 nm. In order to improve the detectable spectral range based on silicon photodetectors, Nazirzadeh M. A. and co-workers used the Au nanoislands formed on the silicon surface by rapidly thermally annealing thin Au layers, so that the silicon photodetector achieved a light response of 2 mA W^{-1} at 1300 nm.[55] (Fig. 4a) Huang and co-workers fabricated silicon photodetectors with a broadband spectral response by femtosecond laser irradiation and titanium hyperdoping. The device can respond to the incident light at 400 nm ~1550 nm, with an average responsivity of 3.42 mA W^{-1} at 1550 nm.[59] Although there are strategies to extend the detectable spectral range of silicon photodetectors beyond 1100 nm, the problem of the low responsivity still needs to be solved.

4.1.2 HgCdTe. HgCdTe is one of the important materials used in the fabrication of infrared detectors. The crystal structure of HgCdTe is a face-centered cubic structure with Hg and Cd atoms arranged alternately (space group $F\bar{4}3m$).[49] The electron mobility and hole mobility of HgCdTe are 10^5 cm^2 V^{-1} s^{-1} and 450 cm^2 V^{-1} s^{-1}, respectively.[60] The low-temperature carrier concentration of HgCdTe can reach 2×10^{15} cm^{-3}.[61] The band gap (0–1.6 eV) of $Hg_{1-x}Cd_xTe$ is tunable.[62,63] Cui and co-workers developed high-sensitivity boron-doped silicon quantum dot/mercury cadmium telluride mid-infrared (MIR) photodetectors (Fig. 4b). The detector has a detectivity of 1.6×10^9 jones at room temperature, a rise time of 224 ns, and a fall time of 580 ns.[56] Wang and co-workers introduced multilayer graphene materials into HgCdTe photodetectors and designed and fabricated uncooled HgCdTe photodetectors with ultrafast and high sensitivity characteristics. The device has a fast response time of 13 ns and a room temperature detection rate of 2×10^{10} jones.[64] In order to achieve high-performance infrared detection, HgCdTe-based infrared photodetectors usually require low-temperature cooling, which inevitably complicates the system and limits integration.[65] High-performance room temperature operation is still a serious challenge for HgCdTe infrared photodetectors.

4.1.3 InGaAs. InGaAs is a common material for commercial near-infrared photodiodes. The crystal structure and space group of InGaAs are the same as those of HgCdTe. InGaAs has a tunable band gap (from 0.36 to 1.425 eV), and its electron mobility and hole mobility are 1200 cm^2 V^{-1} s^{-1} and 300 cm^2 V^{-1} s^{-1}, respectively.[66] At room temperature, the carrier concentration of InGaAs is ~10^{15} cm^{-3}.[67] Suho Park and co-workers have grown InGaAs thin films on InP substrates using the chemical vapor deposition approach and then fabricated InGaAs-based infrared photodetectors (Fig. 4c). The detection rate of the device can reach 4.1×10^{11} jones at room temperature.[57] Li and co-workers fabricated a broadband flexible detector based on the InGaAs/InP PIN structure. The device has a maximum detectivity of 5.18×10^{11} jones at 640–1700 nm.[68] Although InGaAs is competitive in the field of infrared detection, its relatively narrow detection range and large dark current limit its application potential in optical communication.

4.2 2D compounds (van der Waals)

Although the infrared photodetectors based on 3D compounds have been extensively developed, their performances have not been good enough. Hereby, extensive interest has been devoted to the 2D compounds.[11,18,69,70] 2D materials refer to materials in which the carriers can only move freely on the 2D planes.[71] They have a high specific surface area, which can greatly increase the surface area of the interaction with light, thereby improving the detection sensitivity of the photodetector. Photodetectors based on 2D materials can achieve a broadband response (Fig. 5a). The band gap, absorptivity and photoelectric properties of 2D materials can be adjusted by changing the size, shape and composition of materials. For example, the band gap of black phosphorus can change significantly from 0.3 eV (bulk) to 2 eV (monolayer) depending on the number of stacking layers.[72] The characteristics of the carrier motion in the plane of the 2D material make it have a fast response speed and high sensitivity. Under illumination, photons will excite carriers inside the material, which can move freely on the plane inside the materials to form a current. Because these carriers can move quickly in the plane of the 2D materials, they have high sensitivity and fast response speed in photodetectors. For instance, the rise time and decay time of photodetectors based on MoS_2 are 70 μs and 110 μs, respectively.[73] Fig. 5b shows several 2D compounds that have been reported for infrared detection, such as graphene, transition metal sulfides, and black phosphorus. In summary, 2D materials are a large family of materials for infrared photodetectors.

4.2.1 Graphene. Graphene has been used for ultra-wideband photodetectors due to its exceptional crystal structure and physical properties. The crystal structure of graphene is a 2D crystal structure composed of sp^2 hybrid orbitals of

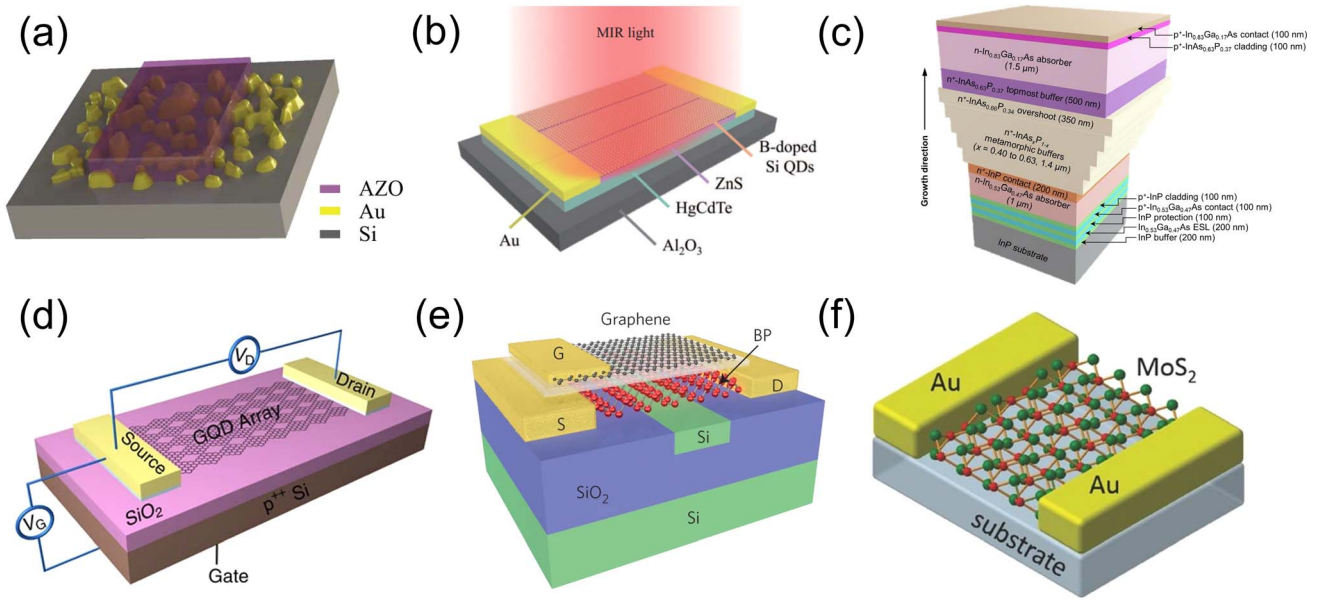

Fig. 4 (a) Schematic diagram of the broad-band NIR Si Schottky photodetector.[55] (b) Schematic illustration of the B-doped Si-QD/MCT device structure.[56] (c) Structure diagram of the photodetector based on the InGaAs material.[57] (d) Schematic diagram of the graphene-based photodetector.[13] (e) Schematic diagram of the black phosphorus infrared photodetector.[14] (f) Schematic diagram of the MoS_2 infrared photodetector.[58]

carbon atoms. Each carbon atom is connected to the other three carbon atoms by a σ bond, and the remaining π electrons form a delocalized large π bond with the π electrons of other carbon atoms. This structure allows electrons to move freely in this region, giving graphene ultrahigh electrical conductivity (2×10^3 S cm^{-1}).[74] Graphene exhibits ultrafast carrier dynamics, and its mobility can reach 200 000 cm^2 V^{-1} s^{-1} at 300 K.[75] Graphene is gapless, which makes its absorption spectrum cover the entire UV to THz spectral regimes.[76] Zhang and co-workers reported a pure single-layer graphene broadband photodetector with a responsivity of 8.61 A W^{-1} (Fig. 4d).[13] Konstantatos and co-workers spin-coated a layer of PbS quantum dots on the surface of graphene as a local grating layer to prepare a graphene-based photodetector.[77] The responsivity of the device can reach 10^7 A W^{-1}. Unfortunately, the small optical absorption of single-layer carbon atoms limits the responsivity of graphene-based photodetectors.[78,79] The integration of colloidal quantum dots in the light absorption layer can improve the responsivity of the graphene photodetector to 10^7 A W^{-1}, but the spectral range of the photodetector is reduced due to the light absorption occurs in the quantum dots.[80]

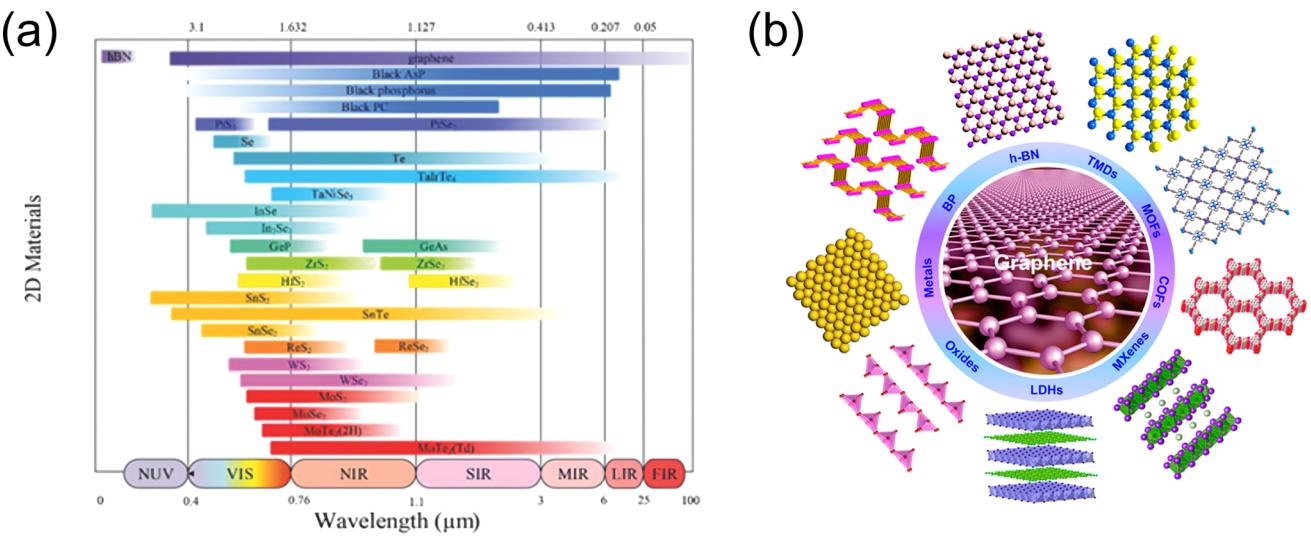

Fig. 5 (a) Comparison of the response wavelength ranges of different 2D materials.[41] (b) Diagram of the crystal structures of the well-known 2D compounds.[71]

4.2.2 Black phosphorus. The phosphorus atoms in the crystal structure of black phosphorus show a hexagonal arrangement. Each phosphorus atom is surrounded by three adjacent phosphorus atoms, forming a planar hexagonal structure. Covalent bonds connect the phosphorus six-membered rings in the crystal structure of black phosphorus to form a 2D layered structure. This layered structure is similar to graphite.[81] The band gap of black phosphorus could be adjusted by the thickness of the layers. The band gap of monolayer black phosphorus is about 2 eV, while the band gap of bulk black phosphorus is about 0.3 eV.[82] At room temperature, the carrier mobility of black phosphorus can reach 1000 $cm^2 V^{-1} s^{-1}$.[83] A wide band gap adjustable range and excellent electrical properties make black phosphorus have great application potential in the field of photodetection.[84] Li and co-workers reported a waveguide-integrated black phosphorus photodetector with a low dark current of 220 nA. At room temperature, the responsivity in the near-infrared region reaches up to 657 mA W^{-1} (Fig. 4e).[14] Guo and co-workers reported a high-gain black phosphorus mid-infrared detector with a responsivity of up to 82 A W^{-1} at a wavelength of 3.39 μm.[85] However, the problem of black phosphorus being unstable and degrading over time when exposed to the environment still needs to be solved.

4.2.3 Transition metal chalcogenides. Transition metal dichalcogenides (TMDs) have unique structures and excellent physical properties. The chemical formula of TMD is MX_2, where M is a transition element and X is a chalcogen element. MoS_2 is a representative semiconductor belonging to the TMDs. Its crystal structure is that the Mo layer in the hexagonal array is sandwiched between the S layers. Strong covalent bonds characterize the Mo–S interaction, while the interaction between the S layers is a van der Waals interaction along the *z*-axis.[86] MoS_2 has a tunable band gap, which can be increased from 1.3 eV (bulk) to 1.8 eV (monolayer).[87] The ultra-wideband multilayer MoS_2 photodetector reported by Xie and co-workers has a responsivity of 50.7 mA W^{-1} in the wavelength range of 445–2717 nm (Fig. 4f).[58] $PtSe_2$ is also a typical TMD material. $PtSe_2$ is a layered structure, in which each layer consists of Pt and Se atoms forming a hexagonal lattice. $PtSe_2$ has a tunable band gap of 0 (bulk) ~1.2 (monolayer) eV.[88] The carrier mobility of $PtSe_2$ can reach 4038 $cm^2 V^{-1} s^{-1}$.[89] The field effect transistor based on $PtSe_2$ prepared by Zhang and co-workers has a responsivity of 0.63 A W^{-1}.[90] In order to further improve the performance of $PtSe_2$-based devices, Xu and co-workers fabricated photodetectors based on the $PtSe_2/SiO_2/Si$ heterojunction. The $PtSe_2/SiO_2/Si$ heterojunction greatly suppresses the dark current and improves the performance of the device. The dark current of the device is as low as 0.12 pA, and the responsivity is as high as 8.06 A W^{-1}.[91] WTe_2 also belongs to the TMD material. Its crystal structure is orthogonal (space group $Pmn2_1$), and each layer of the structure is composed of two layers of tellurium atoms sandwiched between a layer of tungsten atoms.[92] WTe_2 exhibits semimetal properties at room temperature. It has an electron mobility of 3.8×10^4 $cm^2 V^{-1} s^{-1}$ and a hole mobility of 800 $cm^2 V^{-1} s^{-1}$.[93] Xiao and co-workers used laser pulse deposition to deposit large-area WTe_2 films. The responsivity and detectivity of the photodetector based on the WTe_2 thin film are 1.4 mA W^{-1} and 2.3×10^6 jones, respectively.[94] Although TMDs have shown considerable application potential in the infrared detection technology, the growth of large-scale and high-quality TMDs is still challenging.[95]

4.2.4 2D heterostructures. Although photodetectors based on single 2D materials offer significant merits in the field of infrared detection, their performance still requires improvement. For instance, it is challenging for these photodetectors to achieve high responsivity and detectivity in infrared photodetection simultaneously, due to the fact that high responsivity is typically accompanied by large dark currents, thereby diminishing detectivity. By reasonably stacking two-dimensional materials with other materials, 2D/0D heterojunctions, 2D/2D heterojunctions and 2D/3D heterojunctions can be formed. The formation of heterostructures can reduce the shortcomings of a single material and improve the overall performance of the detector. Due to the lack of dangling bonds, two-dimensional materials can form vertical heterojunctions without considering any lattice matching conditions. 2D heterojunction-based photodetectors can combine the detection wavelength bands of two materials, thereby expanding the detection wavelength range. Additionally, by constructing a PN junction, the photovoltaic effect can be enhanced, leading to an improvement in response speed. For example, the response times of GeSe-based photodetectors, InSe-based photodetectors, and WS_2-based photodetectors are 0.7 s, 5 s, and 37.2 ms,[96–98] respectively, while the response times of graphene/InSe/GaSe/graphene-based photodetectors and GaSe/WS_2 heterojunction-based photodetectors can reach 2 μs and 37 μs,[99,100] respectively, which are much faster than those of single-material-based photodetectors. Furthermore, BP heterojunction-based photodetectors can also be used for polarization detection at 1550 nm.[101] Although 2D heterostructures have many merits in the field of infrared photodetection, there are still obstacles to overcome in practical applications. For instance, when transferring 2D materials to build heterostructures, contaminants and defects are inevitably introduced into the material or interface, resulting in degraded device performance.[29]

5. 2D compounds with heterolayers for photodetection

The crystal structures of typical 2D materials, heterolayered materials, and 3D materials are shown in Fig. 6a. Fig. 6b summarizes the responsivity of photodetectors based on typical 2D, heterolayered, and 3D compounds from the UV to MIR region. Compared with other materials, photodetectors based on heterolayered compounds have obvious advantages in the responsivity of this band. The properties of heterolayered materials can be modulated by adjusting the thickness or by introducing different ionic layers. Through the combination of different ion layers, heterolayered compounds can attain high responsivity, high sensitivity, and low power consumption. This

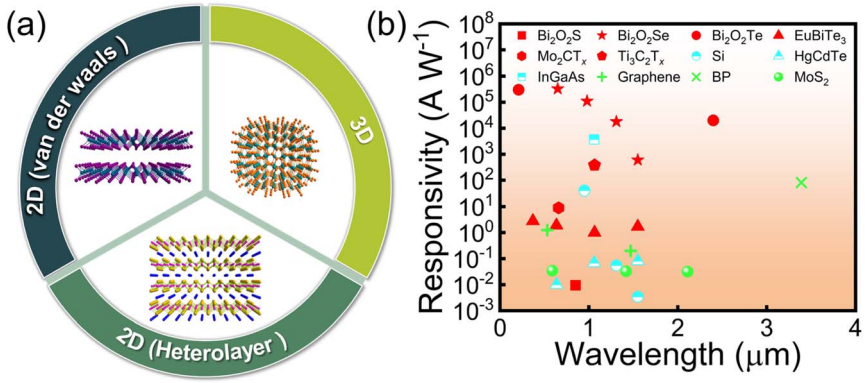

Fig. 6 (a) Comparison of the crystal structures of typical 2D, heterolayered, and 3D compounds. (b) The reported responsivities of photodetectors of typical 2D, heterolayered, and 3D compounds in the UV to MIR region.

kind of versatility is hard to achieve in 2D and 3D materials, providing photodetectors based on heterolayered compounds with significant competitiveness in detecting fields demanding high performance. Heterolayered compounds are formed by the alternating stacking of two or more layers with distinct chemical properties and thereby possess unique traits. It is found that their physical properties are determined by the structures of the constituents and interactions between the layers. Each layer is composed of several thickness of atoms, which enables the 2D feature. Different from the conventional 2D materials (such as graphene, MoS_2, *etc.*), the strong chemical bonding leads to the carriers transfer between the layers, weakening the anisotropic properties and enhancing the 3D properties.[21,102] Examples include $NaCu_4Se_4$ with non-saturating, large, and linear magnetoresistance, the charge density wave material $KLaM_{1-x}Te_4$ (M = Mn and Zn), $[Pb_{3.1}Sb_{0.9}S_4][Au_xTe_{2-x}]$ with anomalous, transverse non-saturating negative magnetoresistance, and $RbEuFe_4As_4$ with superconductivity and ferromagnetism.[103–106] Proper doping in one layer will have a large impact on the other one.

Bi_2O_2Se is a representative semiconductor as a heterolayered material. As shown in Fig. 7, the crystal structure of Bi_2O_2Se consists of alternating positive and negative layers. The positive layer is $[Bi_2O_2]_n^{2n+}$ and the negative layer is $[Se]_n^{2n-}$, with carriers transfer between the layers.[21] In addition, the negative layer can be replaced by elements of the same main group to form other heterolayered materials (Bi_2O_2S, Bi_2O_2Te), thereby expanding the family of heterolayered materials. In the present era, a limited number of heterolayered materials have been used for infrared photodetectors, such as Bi_2O_2X (X = S, Se, Te), $EuMTe_3$ (M = Sb, Bi), and MXene.[25,107–109] Heterolayered materials have attracted the attention of many researchers in the field of infrared photodetection.[108,110–116] Table 1 lists the detailed parameters of the performances of infrared photodetectors based on the typical 2D, heterolayered, and 3D materials. Currently, the detection range of photodetectors based on heterolayered materials is from visible to near-infrared wavelengths. The responsivity of the photodetector based on Bi_2O_2Se in the near-infrared range is 1.1×10^5 A W^{-1},[123] which exceeds that of most near-infrared photodetectors.[127–130] Additionally, $Ti_3C_2T_x$-based and Mo_2CT_x-based photodetectors exhibit commendable performance in the near-infrared range.[25,131] Due to the relatively large band gaps, it is difficult for photodetectors based on Bi_2O_2X (X = S, Se), $Ti_3C_2T_x$, and Mo_2CT_x to achieve mid-far infrared photodetection. Surprisingly, those heterolayered materials (Bi_2O_2Te, $EuSbTe_3$, and $EuBiTe_3$) with narrow band gaps (<0.4 eV) have also not been explored for mid-far infrared photodetection. In the near future, photodetectors based on heterolayered materials for mid-far infrared photodetection need to be explored.

5.1 Layered bismuth oxychalcogenides

In recent years, Bi_2O_2X (X = S, Se, Te), as an emerging 2D material, has received much attention due to its applications in thermoelectric and photoelectric field applications.[110,118,123,132–136] The Bi_2O_2X (X = S, Se, Te) materials have two different crystal structures, Bi_2O_2S belongs to a primitive orthorhombic lattice with a space group *Pnnm*, whereas Bi_2O_2Se and Bi_2O_2Te have a body-centered tetragonal lattice

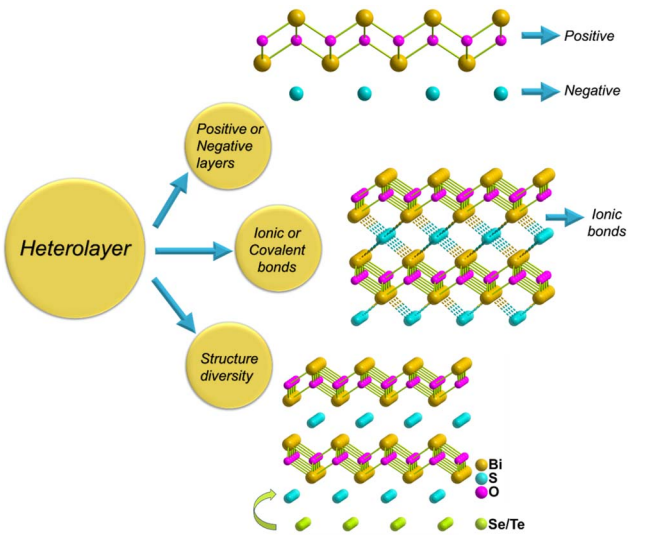

Fig. 7 Scheme of the construction of Bi_2O_2X (X = S, Se, Te).

Table 1 A summary of the performances of the typical 2D materials, heterolayered materials, and 3D materials used for infrared photodetectors[a]

Materials	Dimension	E_g (eV)	R (A W^{-1})	D* (jones)	Res./rec. time	Wavelength (nm)	Ref.
Si	3D	1.12	40.59	3.61×10^{12}	—	950–1550	59
HgCdTe		0–1.6	2.5	2×10^{10}	13 ns	520–4252	64
InGaAs		0.36–1.425	3700	1.01×10^{11}	30/180 ms	1064	117
Graphene	2D	0	0.2	—	—	532–10 310	13
BP		0.3	82	—	—	532–3390	85
MoS_2		0.26	3.25×10^{-2}	1×10^{9}	—	445–2717	58
$PtSe_2$		0.3	0.63	1.95×10^{9}	—	405–808	90
WTe_2		0	1.4×10^{-3}	2.3×10^{6}	—	1064	94
Bi_2O_2S	Heterolayered	1.16	5.9×10^{-2}	6.77×10^{9}	81.9 ms	532	118
Bi_2O_2S		1.5	2.31×10^{-3}	—	0.08 s	250–550	119
Bi_2O_2S		0.67	9.48×10^{-3}	9.96×10^{10}	227.7 ms	850	120
Bi_2O_2Se		0.8	65	3.0×10^{9}	1 ps	300–1700	121
Bi_2O_2Se		0.8	300	—	5.42/2 ms	940–1550	122
Bi_2O_2Se		0.8	3.2×10^{5}	3.28×10^{13}	2.1 μs	650, 1500	123
Bi_2O_2Se		0.8	3.712×10^{3}	3.3×10^{10}	1.77/1.45 ms	300–900	124
Bi_2O_2Te		0.3	3×10^{5}	4×10^{15}	77/126 ms	210–2400	22
$EuBiTe_3$		0.3	1	—	40 ms	370–1550	24
$EuSbTe_3$		0.1	1	2.4×10^{14}	8 ms	325–1550	23
$Ti_3C_2T_x$		0.49–2.15	1.33×10^{-4}	1.46×10^{8}	—	650	125
$Ti_3C_2T_x$		1.53	8.50×10^{2}	3.69×10^{11}	—	1060	126
Mo_2CT_x		—	9	5×10^{11}	500 ms	400–800	25

[a] E_g: band gap, R: responsivity, D*: detectivity, res./rec.: response/recovery.

with space group $I4/mmm$.[110–113] Bi_2O_2S has both ferroelasticity and antiferroelectricity, Bi_2O_2Se exhibits ferroelasticity and piezoelectricity under in-plane strain and Bi_2O_2Te has intrinsic out-of-plane ferroelectricity.[137–139] As shown in Fig. 8a, Bi_2O_2X is connected by ionic bonds, where the $[Bi_2O_2]_n^{2n+}$ positive layer and the $[X]_n^{2n-}$ negative layer are alternately stacked. Bi_2O_2X also has the characteristics of conventional 2D materials, and the band gap value can be changed by adjusting the number of layers.[140] Its unique properties have attracted the attention of many researchers. 'Wei *et al.* proposed a model called the 'zipper model', which explains the structure of 2D Bi_2O_2X well, as shown in Fig. 8b. Each layer contains a $[Bi_2O2]_n^{2n+}$ positive layer and the top $[X]_n^{2n-}$ negative layer. The 50% X on the lower surface of the layer and the 50% X on the upper surface of the bottom $[X]_n^{2n-}$ anion layer are connected by electrostatic force, which is similar to zipper.[107]

5.1.1 Bi_2O_2S. Bi_2O_2S is a layered bismuth oxysulfide family material with a zipper structure. It is stacked by $[Bi_2O_2]_n^{2n+}$ cation layers and $[S]_n^{2n-}$ anion layers.[141] Bi_2O_2S has a tunable band gap (from 0.67 to 1.15 eV). It is loosely structured with a crystal stacking factor of 0.66,[119] which leads to the high carrier mobility of Bi_2O_2S. The electron mobility of monolayer hydrogen passivated Bi_2O_2S at 300 K is 16 447–266 99 cm^2 V^{-1} s^{-1}.[142]

In 2020, Li *et al.* reported the Bi_2O_2S-based photodetector for the first time.[118] Bi_2O_2S nanosheets were synthesized by a one-step hydrothermal method, and Bi_2O_2S thin film photodetectors were prepared by thermal spraying. The response time of the device is 81.9 ms under 532 nm light irradiation. The highest responsivity is 0.059 A W^{-1}, and the highest detectivity is 6.77×10^9 jones.[118] Wang *et al.* synthesized Bi_2O_2S nanosheets and constructed a photoelectrochemical photodetector based on Bi_2O_2S nanosheets. The device has self-healing properties under alkaline conditions, which can prolong the lifetime of photogenerated carriers. Therefore, it has a longer working time. The response time can reach 0.08 s, the response rate can reach 2.31 mA W^{-1}, and it has long-term stability at 0.6 V bias voltage.[119] Rong *et al.* prepared Bi_2O_2S nanoflowers with hierarchical structure by a hydrothermal method (Fig. 8c). The responsivity, detectivity and response time of the infrared photodetector based on Bi_2O_2S nanoflowers are shown in Fig. 8d and e. Under 850 nm infrared light, the responsivity of the Bi_2O_2S nanoflower photodetector is 9.48 mA W^{-1}, the detectivity is 9.96×10^{10} jones, and the response time is 27.74 m.[120]

5.1.2 Bi_2O_2Se. Bi_2O_2Se is the most studied member of the bismuth sulfide oxide semiconductor family by researchers.[143,144] Bi_2O_2Se has a tetragonal crystal structure. The crystal structure of Bi_2O_2Se is composed of alternating stacking of $[Bi_2O_2]_n^{2n+}$ positive layers and $[Se]_n^{2n-}$ negative layers.[145,146] Bi_2O_2Se has a narrow bandgap (0.8 eV). The Hall mobility of Bi_2O_2Se is 29 000 cm^2 V^{-1} s^{-1} at 1.9 K and 450 cm^2 V^{-1} s^{-1} at room temperature.[110–121] In addition, it also has air stability at room temperature.[144] These properties make Bi_2O_2Se show outstanding application potential in the field of infrared detection.[147–153] Peng *et al.* synthesized Bi_2O_2Se nanosheets on mica substrates by chemical vapor deposition. The infrared photodetector based on Bi_2O_2Se nanosheets has high sensitivity in the extremely wide spectral range of 300–1700 nm, high responsivity of 65 A W^{-1} at 1200 nm, and ultrafast light response of 1 ps at room temperature.[121] Chen *et al.* synthesized high-quality, large-area Bi_2O_2Se nanosheets by the CVD method, which realized broadband detection from infrared to THz. Under 940, 1060, 1310 and 1550 nm laser irradiation, the maximum responsivity reached 300, 121, 53 and 58 A W^{-1},

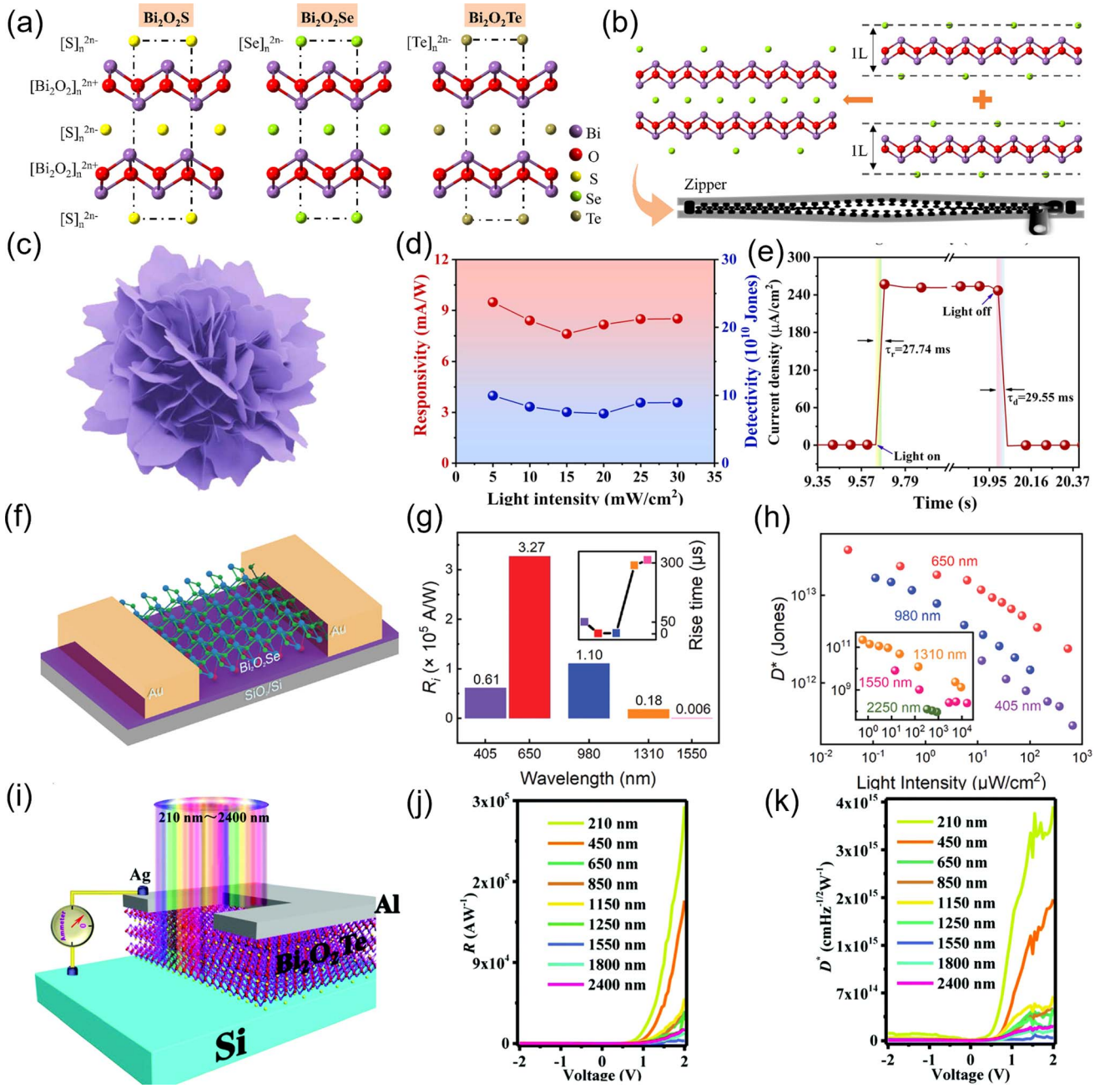

Fig. 8 (a) Crystal structures of Bi_2O_2S, Bi_2O_2Se and Bi_2O_2Te.[140] (b) Scheme of a bilayer Bi_2O_2Se formed by two monolayers and a zipper model.[140] (c) Bi_2O_2S nanoflower diagram.[120] (d) A single magnified photoresponse curve under infrared light illumination with a light intensity of 30 mW cm^{-2}.[120] (e) Responsivity and detectivity as a function of the light intensity.[120] (f) The schematic illustration of the photodetector.[122] (g) The responsivities in wavelengths ranging from 405 to 1550 nm.[123] (h) Variation in detectivity as a function of the light intensity at wavelengths ranging from 405 to 1550 nm.[123] (i) Schematic diagram showing the structure of the photodetector, composed of 2D Bi_2O_2Te and the *n*-Si substrate, with an active area of 4 mm^2 and responding to a broad wavelength between 210 nm and 2.4 μm.[22] (j and k) Responsivity and detectivity against voltage curves at different wavelengths.[22]

respectively.[122] Wei *et al.* synthesized Bi_2O_2Se nanobelts on fluorophlogopite substrates by chemical vapor deposition. A photodetector exhibiting both fast response and low noise was developed by establishing a Schottky barrier between the Bi_2O_2Se nanobelts and the Au electrode (Fig. 8f). The responsivity of the device at 650 nm is 3.2×10^5 A W^{-1} (Fig. 8g). At 650 nm and 1550 nm, the response time is 2.1 μs and 313 μs, and the detectivities are 3.28×10^{13} and 8.07×10^9 jones, respectively (Fig. 8h).[123] Zou *et al.* studied the heat-treated Bi_2O_2Se nanoplates and found that they can also have extremely high air stability in harsh environments. The infrared photodetector based on the heat-treated Bi_2O_2Se nanosheets also has high sensitivity and can work stably at 250 °C. The detectivity reaches 3.3×10^{10} jones and has an ultra-high

responsivity of 3712 A W^{-1}.[124] Nevertheless, Bi_2O_2Se is an indirect bandgap semiconductor with weak light absorption, which results in a significant decline in its photoresponse performance at a wavelength of 1550 nm.[121]

5.1.3 Bi_2O_2Te. As a new member of the bismuth oxysulfide family, Bi_2O_2Te inherits comparable optoelectronic properties to Bi_2O_2Se. Compared with Bi_2O_2Se, Bi_2O_2Te has a lower thermal conductivity, narrower band gap and higher carrier mobility.[154,155] Bi_2O_2Te crystallizes in a space group of *I*4/*mmm* and the crystal structure of Bi_2O_2Te consists of $[Bi_2O_2]^{2+}$ layers and $[Te]^{2-}$ square net layers alternately stacked along the *c*-axis.[156] The ultra-thin Bi_2O_2Te crystals synthesized by the chemical vapor deposition method by Ai *et al.* have ultra-low temperature Hall mobility (>20 000 cm^2 V^{-1} s^{-1}).[157]

Tian *et al.* successfully prepared 2D Bi_2O_2Te films by the magnetron sputtering and rapid annealing approach. Based on Bi_2O_2Te thin films, an ultra-sensitive photodetector for weak light detection was fabricated (Fig. 8i). The device has a wide spectral detection range of 210–2400 nm. The responsivities to deep UV and short-wave infrared are 3×10^5 and 2×10^4 A W^{-1}, respectively (Fig. 8j). The detectivities are 4×10^{15} and 2×10^{14} jones, respectively (Fig. 8k). Due to the saturated absorption characteristics of the surface state of the 2D material, the device exhibits better performance under weak light irradiation than under strong light irradiation.[22] Yang *et al.* synthesized Bi_2Te_3 nanosheets by the solvothermal method and then prepared 2D Bi_2O_2Te nanosheets by low-temperature oxidation. The researchers prepared a quasi-solid-state photoelectrochemical-type (PEC-type) photodetector based on 2D Bi_2O_2Te nanosheets and studied its performance. The PEC-type Bi_2O_2Te photodetector exhibits significant photoresponsive properties in the spectral range from 365 to 850 nm. Its responsivity at 365 nm is up to 20.5 mA W^{-1}.[154]

5.2 $EuMTe_3$ (M = Bi, Sb)

$EuMTe_3$ is a layered bimetallic telluride with a low band gap value. $EuMTe_3$ crystallizes in a layered structure in the *Pmmn* space group. As shown in Fig. 9a, it consists of a stacked Eu–Te–M slab and a Te atomic layer, where the Te atomic layer is sandwiched between the Eu–Te–M slab. Inside the Eu–Te–M plate, M–Te and Eu–Te zigzag network structures are tightly bonded.[108] In 2015, Niu *et al.* synthesized ternary tellurides $EuMTe_3$ (M = Bi, Sb) by the low-temperature flux method and studied their properties. The optical band gaps of $EuSbTe_3$ and $EuBiTe_3$ are 0.1 eV and 0.3 eV, respectively.[108]

5.2.1 $EuBiTe_3$. Niu *et al.* prepared $EuBiTe_3$ by the flux method, and obtained $EuBiTe_3$ flakes from $EuBiTe_3$ crystals by the transparent tape method, and deposited Au electrodes on the surface of $EuBiTe_3$. Based on $EuBiTe_3$ flakes, photodetectors were fabricated on $EuBiTe_3$ flakes. Fig. 9b and c show that the device has a broadband response at 370–1550 nm with a responsivity greater than 1 A W^{-1}, and the performance does not change significantly after exposure to air at room temperature for three months.[24]

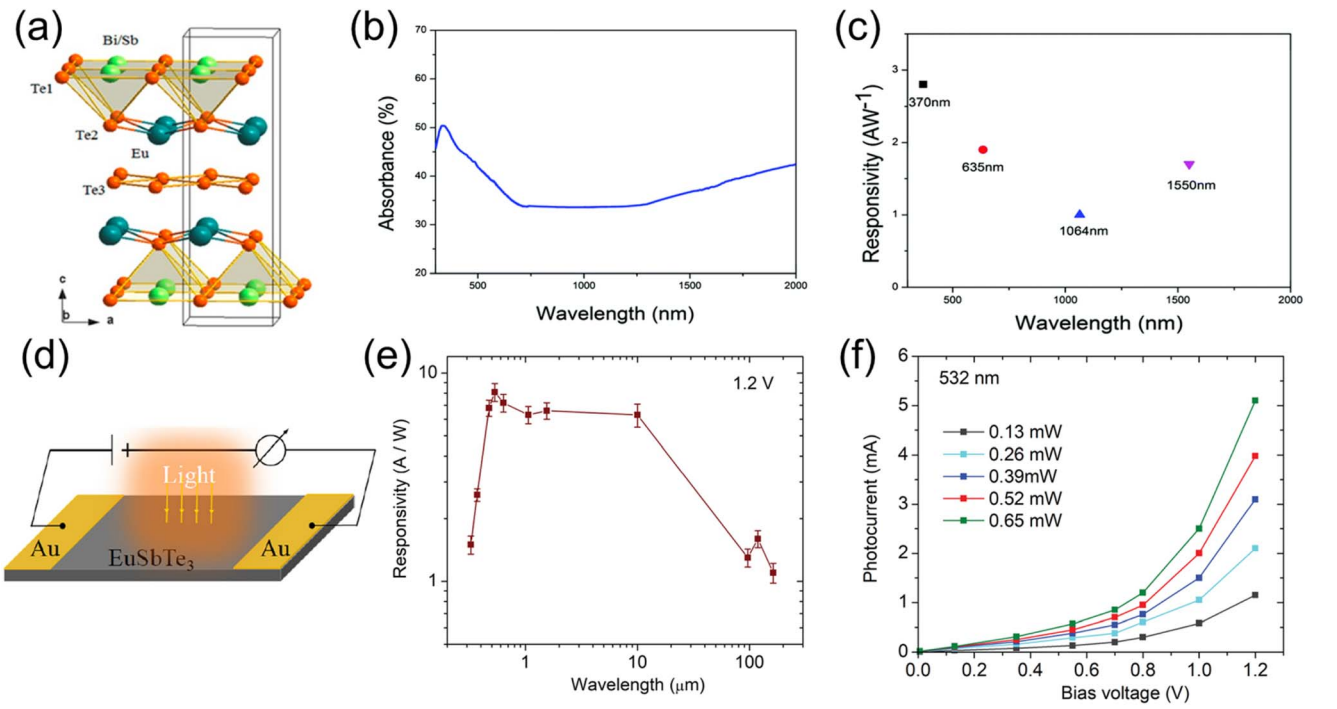

Fig. 9 (a) The schematic illustration of the crystal structure of $EuMTe_3$ (M = Bi, Sb).[108] (b) RT *ab*-plane optical absorbance spectrum of $EuBiTe_3$ crystals.[24] (c) The responsivity for our $EuBiTe_3$ detectors under illumination with wavelengths from UV to near-infrared (NIR) based on the same device.[24] (d) The schematic diagram of the $EuSbTe_3$ photodetector.[23] (e) For applied bias 1.2 V, the available ultra-broadband photoresponsivities from UV to THz at various illuminations at 325 nm, 370 nm, 473 nm, 532 nm, 635 nm, 1064 nm, 1550 nm, 10.6 μm, 96.5 μm, 118.8 μm and 163 μm, respectively.[23] (f) The photocurrent as a function of applied bias voltage under 532 nm illumination.[23]

5.2.2 $EuSbTe_3$. Niu *et al.* further prepared $EuSbTe_3$ single crystals by the flux method and then peeled out $EuSbTe_3$ flakes using the transparent tape method, and fabricated photodetectors based on $EuSbTe_3$ flakes. The structure of the $EuSbTe_3$ photodetector is shown in Fig. 9d. The device has excellent direct photosensitive performance in the UV-THz wavelength range. Fig. 9e and f show the photoresponsivity of the device is greater than 1 A W^{-1} in the THz wavelength range, under the illumination of 532 nm, the photocurrent increases rapidly and nonlinearly with the increase of bias voltage. And it can maintain stable performance after three months at room temperature in air.[23]

5.3 MXenes

MXene is a new type of 2D crystal compound with a hexagonal structure and novel properties.[158] The general formula of MXene is $M_{n+1}X_n$ or $M_{n+1}X_nT_x$ ($n = 1, 2, 3$), where M is a transition metal (M = Sc, Ti, Ta, Hf, Zr, V, Nb, Cr, Mo), X is carbon or nitrogen, and T_x represents functional groups, such as –O, –OH, –F and –Cl. MXenes have excellent light transmittance, and the light transmittance of many MXenes can reach more than 90%.[159–161] It also has extremely conductivity, and its composite with graphene exceeds the conductivity of commercial indium tin oxide films. By compositing with a small amount of graphene, MXene/graphene composites with a conductivity of 9.5×10^4 S cm^{-1} can be obtained.[162] These unique properties have made them highly sought after in the field of photodetection.[109,163–171] However, the extremely narrow band gap (0–0.1 eV) of MXene containing –F, –OH and –O terminal groups limits its application in the field of photodetectors.[172]

As a representative material of the MXene family, $Ti_3C_2T_x$ has high electrical conductivity, and the conductivity of $Ti_3C_2T_x$ thin films reaches 8000–25 000 S cm^{-1}.[158,173] Furthermore, the material exhibits high transparency, and a single $Ti_3C_2T_x$ layer can transmit about 97% of visible light.[174] The structure of $Ti_3C_2T_x$ is shown in Fig. 10a.[114,115] Hu *et al.* prepared semiconducting $Ti_3C_2T_x$ MXene by grafting dodecyl ($-C_{12}H_{26}$) groups on $Ti_3C_2T_x$ MXene materials. The band gap (from 0.49 to 2.15 eV) can be changed by adjusting the number of layers of the semiconductor $Ti_3C_2T_x$ MXene. Fig. 10b shows the *I–V* curves of $Ti_3C_2T_x$-based infrared photodetectors under laser irradiation at 1064 nm with different optical power densities. Under the irradiation of a 1064 nm laser, the responsivity and detectivity can reach 1.33×10^{-4} A W^{-1} and 1.46×10^8 jones, respectively (Fig. 10c).[125] Liu also found that $Ti_3C_2T_x$-based infrared photodetectors generate polarized photocurrent at zero bias under the irradiation of a 1064 nm laser.[175] In a separate study, Hu *et al.* prepared the semiconductor $Ti_3C_2T_x$ MXene (S-$Ti_3C_2T_x$) with a band gap of 1.53 eV using a benzenesulfonic acid group ($-phSO_3H$) as a surface functional group. The phenylsulfonic acid group modified $Ti_3C_2T_x$ MXene (S-$Ti_3C_2T_x$)-based flexible photodetector has a maximum responsivity of 8.50×10^2 A W^{-1} and a detectivity of 3.69×10^{11} jones under 1064 nm laser irradiation.[126]

As another member of the MXene family, Mo_2CT_x has high electrical conductivity and optical properties and can achieve a broadband response in the UV and near-infrared bands.[116] The structure of Mo_2CT_x is shown in Fig. 10d. The Mo_2CT_x material can achieve high sensitivity detection of infrared light, and the detection sensitivity is even higher than that of HgCdTe and InGaAs. The photodetector based on the Mo_2CT_x material obtains a weak optical response in the range of 325–1064 nm, the responsivity is 9 A W^{-1} and the detectivity is 5×10^{11} jones under 660 nm laser irradiation (Fig. 10e and f).[25] The above studies have proved the feasibility of Mo_2CT_x materials for infrared photodetection. At present, the most studied is still the infrared photodetector based

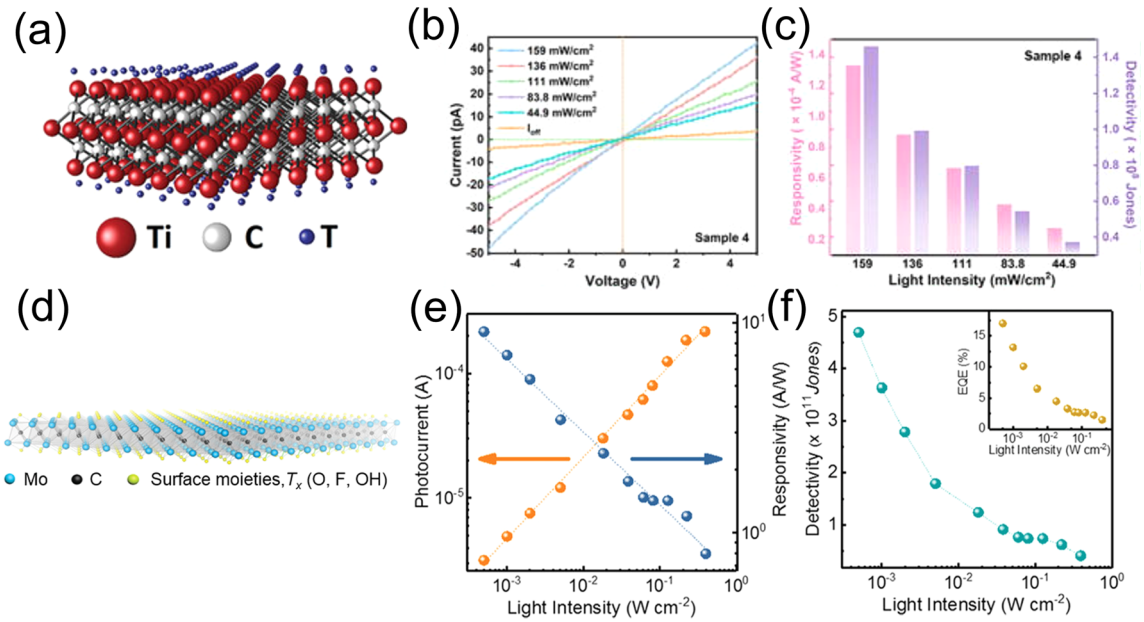

Fig. 10 (a) $Ti_3C_2T_x$ structure diagram.[109] (b) *I–V* curves under laser irradiation of 1064 nm with different optical power densities.[125] (c) The detectivity and responsivity under different optical power densities at 1064 nm.[125] (d) Structure diagram of Mo_2CT_x.[25] (e) Responsivity of the photodetector as a function of different light intensities.[25] (f) The detectivity of the photodetector as a function of different light intensities.[25]

on $Ti_3C_2T_x$. There are relatively few studies on other members of the MXene family applied to infrared photodetectors.

6. Application of infrared photodetectors

6.1 Cell detection

So far, most cancer patients have died of metastatic tumors (CTC). Therefore, the development of high-performance sensing systems for CTC measurement is very important for early diagnosis, prognosis and accurate treatment of cancer patients.[176] Photoelectrochemical (PEC) immunosensing technology is a new type of CTC detection technology. Compared with traditional CTC detection techniques (chromatography-mass spectrometry, enzyme-linked immunosorbent assay, and fluorescence spectroscopy),[177–179] the PEC immunosensing system is more sensitive and stable for the detection of CTCs.[180] The core of the PEC immunosensor is the photosensitive material.[181] Xu and co-workers used Bi_2O_2S nanoflowers as photosensitive elements to construct a near-infrared photoelectrochemical (PEC) biosensing interface that can be excited with an 808 nm laser. The mechanism of the near-infrared PEC biosensor interface for detecting tumor cells is shown in Fig. 11a. The aptamer was immobilized on the surface of AuNPs/Bi_2O_2S/ITO, which can selectively capture tumor cells. When the tumor cells were captured on the AuNPs/Bi_2O_2S/ITO surface, the photocurrent of the PEC biosensor interface decreased accordingly. The change of current achieves the quantitative detection of tumor cells.[182]

6.2 Monitoring

In laser operation, the monitoring of optical power density is particularly important. For example, the femtosecond laser is needed for myopia recovery surgery. The femtosecond laser has the advantages of high instantaneous power, short pulse time and accurate focusing range.[184] Hu and co-workers used $Ti_3C_2T_x$ MXene as the conductive electrode and RAN films as the active material to design an infrared photodetector based on the $Ti_3C_2T_x$-RAN heterostructure. During surgery, the monitor platform is adjusted to the same height as the eye. When the laser is turned on, the power density monitoring system composed of $Ti_3C_2T_x$-RAN converts the optical signal into a current signal. After being amplified by the *I–V* circuit, the current signal is collected by the microprocessor for processing and conversion. Finally, the optical power density of the laser is displayed on the

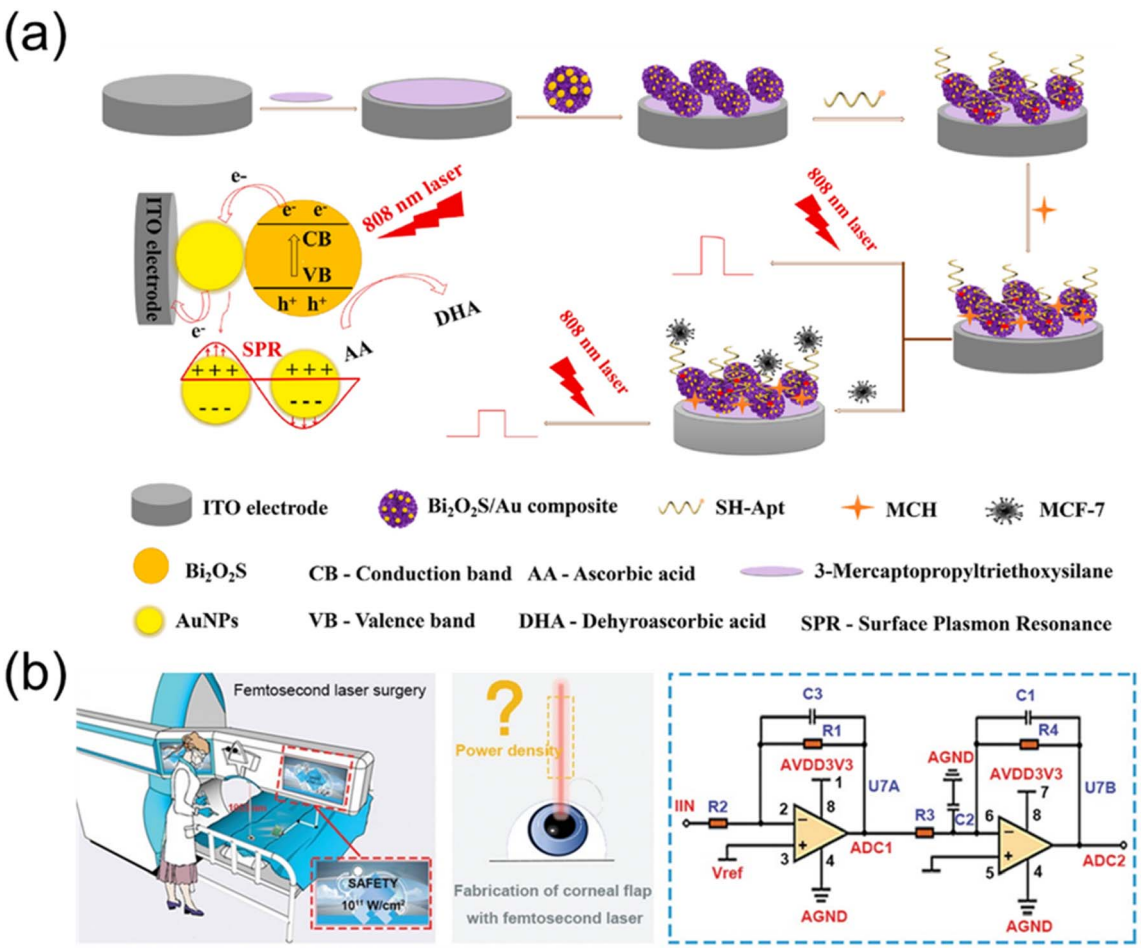

Fig. 11 (a) The fabrication of the PEC aptamer sensor and the detection mechanism of tumor cells.[182] (b) $Ti_3C_2T_x$-RAN photodetector monitors laser density display and laser density monitoring system circuit diagram during femtosecond laser surgery.[183]

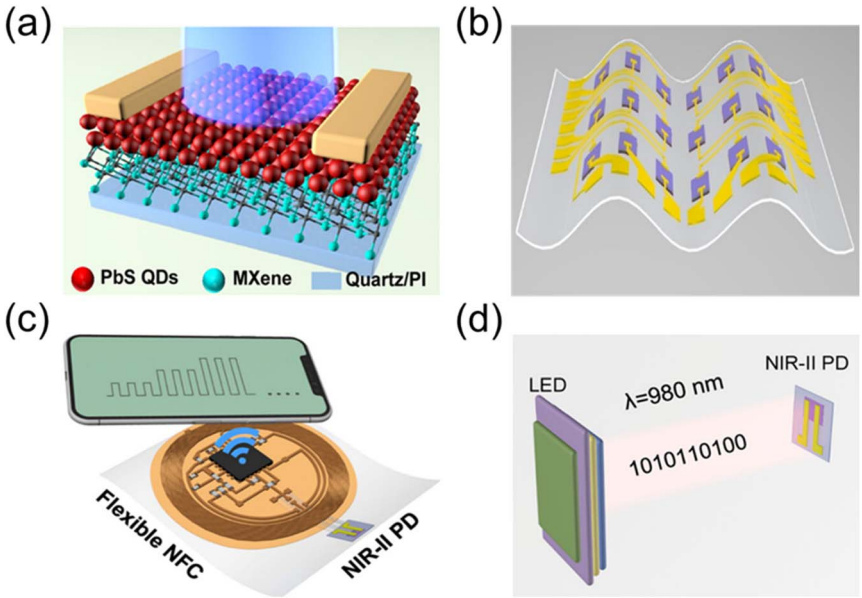

Fig. 12 (a) MXene/PbS infrared photodetector schematic diagram.[185] (b) A skin-like bilayer photodetector array was prepared on the PI substrate.[185] (c) A schematic diagram of a wireless photodetection system using flexible NFC and NIR-II photodetectors.[185] (d) The schematic diagram of optical communication through NIR-II light.[185]

screen. The device can monitor the optical power density of the laser during myopia surgery to prevent excessive laser power from causing damage to the eyes (Fig. 11b).[183]

6.3 Optical communication

Flexible infrared photodetectors have great advantages in optical communication. By combining MXene ($Ti_3C_2T_x$) and photosensitive lead sulfide quantum dots, skin-like photodetectors and arrays with simple bilayer configurations are fabricated. The separation of photocarriers is highly promoted at the interface of the bilayer, and efficient transmission is achieved between the spatial separation layers. A double-layer photodetector based on MXene/PbS was obtained by spin-coating MXene and lead sulfide quantum dots on quartz and PI substrates, and then evaporating silver electrodes (Fig. 12a). Fig. 12b is a schematic diagram of a two-layer photodetector array based on MXene/PbS. The flexible wireless NFC system is integrated with a MXene/PbS-based double-layer photodetector array (Fig. 12c). The NFC system can store and wirelessly transmit distance-containing information by NIR-II light reflected from fingers or other objects. When the finger is closer to the sensor, more light will be reflected on the sensor and produce higher photocurrent. When the hand leaves, the current decreases due to less light irradiated on the sensor. The transmission of information is realized by encoding and analyzing the change of current (Fig. 12d).[185]

7. Outlook of heterolayered materials for infrared detectors

Heterolayered materials have great research potential in the field of optoelectronics. In fact, there is a large number of heterolayered compounds in the inorganic crystal structure database (ICSD) such as $RETe_2$, $RETe_3$ (RE = Y, La, Ce, Pr, Nd, Sm, Gd, Tb, Dy, Ho, Er and Tm), MX_2 (M = Eu, Gd; X = Ge, Si) and so on.[186–188] $RETe_3$ has a heterolayered structure with a unit cell consisting of two RE-Te plates separated by two Te sheets.[187] $RETe_3$ has a small effective mass and very high carrier mobility, and $GdTe_3$ has the highest mobility among all known 2D layered magnetic materials. The electron mobility is beyond 60 000 $cm^2\ V^{-1}\ s^{-1}$.[189] Coupled with silicene and germanene, Eu and Gd formed a new 2D RE compounds MX_2 (M = Eu, Gd; X = Ge, Si). The stoichiometric MX_2 has layered structure. In MX_2, Eu or Gd forms the triangular lattice, while silicene or germanene forms the 2D honeycomb network.[188] $EuGe_2$ is a bipolar magnetic semiconductor with a band gap of 0.55 eV, and its carrier mobility can be up to $10^4\ cm^2\ V^{-1}\ s^{-1}$.[190,191] $EuSi_2$ is a semiconductor with an indirect surface band gap of 0.45 eV.[192] $GdGe_2$ is a ferromagnetic half-semiconductor and an indirect band gap of 0.55 eV.[193] The narrow bandgaps of MX_2 allow them to be excited by infrared light, and they also have high enough carrier mobility. It is foreseeable that the research of heterolayered compounds in the field of infrared photodetection will definitely have vigorous development in the near future.

8. Conclusions

In summary, we begin by outlining the evolution of materials with 3D and 2D structures that are apt for infrared photodetectors. Then we introduced the research progress of infrared photodetectors based on heterolayered materials. Photodetectors based on heterolayered materials have been reported to have broadband detection, THz detection, polarization-sensitive light detection, *etc.* Bi_2O_2S has self-healing

properties under alkaline conditions to extend the lifetime of photogenerated carriers. Bi_2O_2Se-based photodetectors have a broadband response from UV to THz, with high responsivity and detectivity. However, due to its indirect bandgap semiconductor and weak light absorption, its optical response at 1550 nm is significantly reduced. Bi_2O_2Te has polarization-sensitive photodetection properties, but its synthesis process still needs to be optimized. Although $EuMTe_3$ (M = Sb, Bi) has extremely high stability at room temperature and can maintain its performance after being placed in air at room temperature for 3 months, there are still few studies on them. MXene can achieve a fast response and has high chemical stability and thermal stability. By introducing surface functional groups to regulate the band gap of $Ti_3C_2T_x$, its response in the infrared band is realized. Moreover, it has high transparency and flexibility, which provides conditions for the preparation of transparent and flexible/stretchable electronic devices. However, except for $Ti_3C_2T_x$, other members of the MXene family have been studied less in the field of infrared photodetection.

Although heterolayered materials have been extensively studied, there is still considerable research value and scope for improvement in the field of infrared photodetection.

(1) Firstly, many heterolayered materials with suitable band gaps are identified in the inorganic crystal structure database, such as $RETe_2$, $RETe_3$ (RE = Y, La, Ce, Pr, Nd, Sm, Gd, Tb, Dy, Ho, Er, and Tm), MX_2 (M = Eu, Gd; X = Ge, Si), *etc.* Investigations of these compounds for detectors are worthy to be conducted. Secondly, the construction of different 2D constituents could be designed to form new compounds. The functional layers need to have comparable lattice parameters and strong bonds between the outermost ions, leading to new materials with promising properties. For instance, the combination of superconducting layers and magnetic layers lead to the formation of new magnetic superconductors, like $RbEuFe_4As_4$ with a superconducting [FeAs] layer and a ferromagnetic Eu layer.[105]

(2) Current research on infrared photodetectors made of heterolayered materials mainly focuses on the NIR wavelength band, while studies on the MIR and far-infrared (FIR) wavelength bands have lagged behind. The performance of the heterolayered material photodetector can be optimized by adjusting the physical properties of the semiconductors. Considering the doping elements, different elements can introduce new energy levels in the forbidden band, facilitating the generation and separation of photogenerated carriers and improving photoelectric performance. As for the doping concentration, a too low concentration may not fully introduce the needed energy levels, leading to insufficient generation and separation efficiency of photogenerated carriers, affecting light absorption and photoelectric conversion efficiency of the material. However, an overly high concentration may cause lattice distortion, reduce carrier mobility, and impede charge transport, adversely affecting the photoelectric performance. An appropriate doping concentration can optimize the energy band structure of heterolayered materials, enhance charge separation and transport efficiency, boost light absorption, and significantly enhance photoelectric performance. As for doping sites, doping at specific lattice sites can introduce new energy levels, altering the positions and distributions of the valence band maximum and conduction band minimum, directly influencing the material's light absorption and charge transport properties. Meanwhile, for the heterolayered materials, when the doping site is close to the interface, it may change the band bending and charge distribution at the interface, influencing the charge transfer and separation efficiency at the interface and thereby affecting the photoelectric performance.

(3) The response speed of infrared photodetectors based on heterolayered materials is frequently sluggish. A fast response can be attained by optimizing the carrier mobility of the material, enhancing the electrodes of the device, and establishing a heterojunction structure. Regarding carrier mobility, optimizing the growth process can improve crystal quality and minimize the presence of impurities and defects. This is because impurities and defects scatter the carriers, impeding their free movement and thereby reducing their mobility. Optimizing the electrode by selecting an electrode material with high conductivity, such as a metal with excellent conductivity, can lower the electrode resistance, accelerate the transport of carriers within the electrode, and thus shorten the response time. Appropriately reducing the thickness of the electrode can decrease the resistance and capacitance of the electrode and mitigate the delay of carrier transmission. The utilization of a rational electrode structure can increase the contact area between the electrode and the detection material, enhancing the carrier collection efficiency, and decreasing the response time. Appropriate electrode spacing and arrangement also contribute to reducing the effects of capacitance and resistance. For heterojunction structures, choosing two materials with matching band structures, such as combining a material with a wide bandgap and high carrier mobility with a material with a narrow bandgap and a high optical absorption coefficient, can simultaneously achieve high responsivity and fast response time. Precise regulation of the thickness of each layer within the heterojunction can optimize the distribution and intensity of the built-in electric field and expedite the separation and transport of carriers. On the other hand, the response time of the photodetector is restricted by the bandwidth. When the bandwidth is increased by narrowing the width of the intrinsic region and downsizing the device, the light absorption of the material is affected, leading to a decrease in responsivity. The light propagation direction of the waveguide-coupled photodetector is perpendicular to the transmission direction of the carrier, reducing the mutual constraint between the response time and the responsivity. High responsivity and fast response speed of photodetectors can be optimized by preparing waveguide-coupled photodetectors.

All in all, heterolayered materials have great research potential in the field of infrared photodetection. While strides have been made in the development of infrared photodetectors using 2D materials, several challenges persist: (1) existing infrared photodetectors, despite their high sensitivity, encounter issues of signal interference and excessive background noise in certain environments. This compromises the accuracy and stability of these detectors. (2) The production of two-dimensional material infrared photodetectors presents its

own set of challenges. The complex manufacturing process and high production costs hinder their large-scale application. (3) The requirements for infrared photodetectors vary across different fields, such as military, security, medical, and environmental protection. This necessitates the development of detectors with broad adaptability.

Data availability

No primary research results have been included and no new data were generated or analysed as part of this review.

Author contributions

Hao Gu and Tianshuo Zhang wrote the review and contributed equally. Yunluo Wang and Tianrui Zhou revised the manuscript. Haijie Chen developed the concept and edited this review.

Conflicts of interest

There are no conflicts to declare.

Acknowledgements

This work was supported by the National Natural Science Foundation of China (22101045).

References

1 J. Cao, B. Jiang, H. Jiao, X. Niu, J. Zhang, Z. Zhang, X. Cheng and Z. Wang, A Dichroic Beamsplitter for the Laser Protection of Infrared Detectors, *Coatings*, 2022, **12**, 1861.
2 T. Zhang, C. Ling, X. Wang, B. Feng, M. Cao, X. Xue, Q. Xue, J. Zhang, L. Zhu and C. Wang, Six-arm Stellat Dendritic-PbS Flexible Infrared Photodetector for Intelligent Healthcare Monitoring, *Adv. Mater. Technol.*, 2022, **7**, 2200250.
3 S. Kim, Y. T. Lim, E. G. Soltesz, A. M. De Grand, J. Lee, A. Nakayama, J. A. Parker, T. Mihaljevic, R. G. Laurence and D. M. Dor, Near-infrared fluorescent type II quantum dots for sentinel lymph node mapping, *Nat. Biotechnol.*, 2004, **22**, 93–97.
4 N. Ding, Y. Wu, W. Xu, J. Lyu, Y. Wang, L. Zi, L. Shao, R. Sun, N. Wang and S. Liu, A novel approach for designing efficient broadband photodetectors expanding from deep ultraviolet to near infrared, *Light: Sci. Appl.*, 2022, **11**, 91.
5 A. Rogalski, History of infrared detectors, *Opto-Electron. Rev.*, 2012, **20**, 279–308.
6 E. Putley, Thermal detectors, *Optical and Infrared Detectors*, 2005, pp. 71–100.
7 W. Ma, Y. Gao, L. Shang, W. Zhou, N. Yao, L. Jiang, Q. Qiu, J. Li, Y. Shi, Z. Hu and Z. Huang, Ultrabroadband Tellurium Photoelectric Detector from Visible to Millimeter Wave, *Adv. Sci.*, 2022, **9**, 2103873.
8 L. Wang, C. Liu, X. Chen, J. Zhou, W. Hu, X. Wang, J. Li, W. Tang, A. Yu, S.-W. Wang and W. Lu, Toward Sensitive Room-Temperature Broadband Detection from Infrared to Terahertz with Antenna-Integrated Black Phosphorus Photoconductor, *Adv. Funct. Mater.*, 2017, **27**, 1604414.
9 S. Bianconi and H. Mohseni, Recent advances in infrared imagers: toward thermodynamic and quantum limits of photon sensitivity, *Rep. Prog. Phys.*, 2020, **83**, 044101.
10 G. Rao, X. Wang, Y. Wang, P. Wangyang, C. Yan, J. Chu, L. Xue, C. Gong, J. Huang, J. Xiong and Y. Li, Two-dimensional heterostructure promoted infrared photodetection devices, *InfoMat*, 2019, **1**, 272–288.
11 J. Yao and G. Yang, 2D material broadband photodetectors, *Nanoscale*, 2020, **12**, 454–476.
12 L. Zhang, N. Wang and Y. Li, Design, synthesis, and application of some two-dimensional materials, *Chem. Sci.*, 2023, **14**, 5266–5290.
13 B. Y. Zhang, T. Liu, B. Meng, X. Li, G. Liang, X. Hu and Q. J. Wang, Broadband high photoresponse from pure monolayer graphene photodetector, *Nat. Commun.*, 2013, **4**, 1811.
14 N. Youngblood, C. Chen, S. J. Koester and M. Li, Waveguide-integrated black phosphorus photodetector with high responsivity and low dark current, *Nat. Photonics*, 2015, **9**, 247–252.
15 H. Wang, C. Zhang, W. Chan, S. Tiwari and F. Rana, Ultrafast response of monolayer molybdenum disulfide photodetectors, *Nat. Commun.*, 2015, **6**, 8831.
16 D. H. Kang, M. S. Kim, J. Shim, J. Jeon, H. Y. Park, W. S. Jung, H. Y. Yu, C. H. Pang, S. Lee and J. H. Park, High-performance transition metal dichalcogenide photodetectors enhanced by self-assembled monolayer doping, *Adv. Funct. Mater.*, 2015, **25**, 4219–4227.
17 L. Li, G. J. Ye, V. Tran, R. Fei, G. Chen, H. Wang, J. Wang, K. Watanabe, T. Taniguchi and L. Yang, Quantum oscillations in a two-dimensional electron gas in black phosphorus thin films, *Nat. Nanotechnol.*, 2015, **10**, 608–613.
18 X. Chen, X. Lu, B. Deng, O. Sinai, Y. Shao, C. Li, S. Yuan, V. Tran, K. Watanabe, T. Taniguchi, D. Naveh, L. Yang and F. Xia, Widely tunable black phosphorus mid-infrared photodetector, *Nat. Commun.*, 2017, **8**, 1672.
19 C. O. Kim, S. Kim, D. H. Shin, S. S. Kang, J. M. Kim, C. W. Jang, S. S. Joo, J. S. Lee, J. H. Kim, S.-H. Choi and E. Hwang, High photoresponsivity in an all-graphene p–n vertical junction photodetector, *Nat. Commun.*, 2014, **5**, 3249.
20 C. K. Kanade, H. Seok, V. K. Kanade, K. Aydin, H.-U. Kim, S. B. Mitta, W. J. Yoo and T. Kim, Low-temperature and large-scale production of a transition metal sulfide vertical heterostructure and its application for photodetectors, *ACS Appl. Mater. Interfaces*, 2021, **13**, 8710–8717.
21 A. P. Balan, A. B. Puthirath, S. Roy, G. Costin, E. F. Oliveira, M. A. S. R. Saadi, V. Sreepal, R. Friedrich, P. Serles, A. Biswas, S. A. Iyengar, N. Chakingal, S. Bhattacharyya, S. K. Saju, S. C. Pardo, L. M. Sassi, T. Filleter, A. Krasheninnikov, D. S. Galvao, R. Vajtai, R. R. Nair and P. M. Ajayan, Non-van der Waals quasi-2D materials;

recent advances in synthesis, emergent properties and applications, *Mater. Today*, 2022, **58**, 164–200.

22 P. Tian, H. Wu, L. Tang, J. Xiang, R. Ji, S. P. Lau, K. S. Teng, W. Guo, Y. Yao and L.-J. Li, Ultrasensitive broadband photodetectors based on two-dimensional Bi2O2Te films, *J. Mater. Chem. C*, 2021, **9**, 13713–13721.

23 Y. Y. Niu, D. Wu, Y. Q. Su, H. Zhu, B. Wang, Y. X. Wang, Z. R. Zhao, P. Zheng, J. S. Niu, H. B. Zhou, J. Wei and N. L. Wang, Uncooled EuSbTe3 photodetector highly sensitive from ultraviolet to terahertz frequencies, *2D Mater.*, 2017, **5**, 011008.

24 Y. Niu, B. Wang, J. Chen and D. Wu, Ultra-broadband and highly responsive photodetectors based on a novel EuBiTe3 flake material at room temperature, *J. Mater. Chem. C*, 2018, **6**, 713–716.

25 D. B. Velusamy, J. K. El-Demellawi, A. M. El-Zohry, A. Giugni, S. Lopatin, M. N. Hedhili, A. E. Mansour, E. D. Fabrizio, O. F. Mohammed and H. N. Alshareef, MXenes for Plasmonic Photodetection, *Adv. Mater.*, 2019, **31**, 1807658.

26 Q. Qiu and Z. Huang, Photodetectors of 2D Materials from Ultraviolet to Terahertz Waves, *Adv. Mater.*, 2021, **33**, 2008126.

27 Z. Cheng, T. Zhao and H. Zeng, 2D Material-Based Photodetectors for Infrared Imaging, *Small Sci.*, 2022, **2**, 2100051.

28 J. Zha, M. Luo, M. Ye, T. Ahmed, X. Yu, D. H. Lien, Q. He, D. Lei, J. C. Ho and J. Bullock, Infrared photodetectors based on 2D materials and nanophotonics, *Adv. Funct. Mater.*, 2022, **32**, 2111970.

29 X. Guan, X. Yu, D. Periyanagounder, M. R. Benzigar, J. K. Huang, C. H. Lin, J. Kim, S. Singh, L. Hu and G. Liu, Recent progress in short-to long-wave infrared photodetection using 2D materials and heterostructures, *Adv. Opt. Mater.*, 2021, **9**, 2001708.

30 Y. Liu, X. Yi, N. J. Bailey, Z. Zhou, T. B. O. Rockett, L. W. Lim, C. H. Tan, R. D. Richards and J. P. R. David, Valence band engineering of GaAsBi for low noise avalanche photodiodes, *Nat. Commun.*, 2021, **12**, 4784.

31 J. Chen, J. Chen, X. Li, J. He, L. Yang, J. Wang, F. Yu, Z. Zhao, C. Shen, H. Guo, G. Li, X. Chen and W. Lu, High-performance HgCdTe avalanche photodetector enabled with suppression of band-to-band tunneling effect in mid-wavelength infrared, *npj Quantum Mater.*, 2021, **6**, 103.

32 J. Li, A. Dehzangi, G. Brown and M. Razeghi, Mid-wavelength infrared avalanche photodetector with AlAsSb/GaSb superlattice, *Sci. Rep.*, 2021, **11**, 7104.

33 G. Wu, R. Fu, J. Chen, W. Yang, J. Ren, X. Guo, Z. Ni, X. Pi, C. Z. Li and H. Li, Perovskite/Organic Bulk-Heterojunction Integrated Ultrasensitive Broadband Photodetectors with High Near-Infrared External Quantum Efficiency over 70%, *Small*, 2018, **14**, 1802349.

34 Q. Zhang, D. Liu, Z. Wang, P. Dang, H. Lian, G. Li and J. Lin, LaMgGa11O19: Cr3+, Ni2+ as blue-light excitable near-infrared luminescent materials with ultra-wide emission and high external quantum efficiency, *Adv. Opt. Mater.*, 2023, **11**, 2202478.

35 W. Yin, J. Yang, K. Zhao, A. Cui, J. Zhou, W. Tian, W. Li, Z. Hu and J. Chu, High responsivity and external quantum efficiency photodetectors based on solution-processed Ni-doped CuO films, *ACS Appl. Mater. Interfaces*, 2020, **12**, 11797–11805.

36 V. Mackowiak, J. Peupelmann, Y. Ma and A. Gorges, *NEP – Noise Equivalent Power*, Thorlabs, Inc, 2015, p. 56.

37 L. Huang, W. C. Tan, L. Wang, B. Dong, C. Lee and K.-W. Ang, Infrared black phosphorus phototransistor with tunable responsivity and low noise equivalent power, *ACS Appl. Mater. Interfaces*, 2017, **9**, 36130–36136.

38 R. Tauk, F. Teppe, S. Boubanga, D. Coquillat, W. Knap, Y. Meziani, C. Gallon, F. Boeuf, T. Skotnicki and C. Fenouillet-Beranger, Plasma wave detection of terahertz radiation by silicon field effects transistors: Responsivity and noise equivalent power, *Appl. Phys. Lett.*, 2006, **89**, 253511.

39 G. H. Shin, J. Park, K. J. Lee, G.-B. Lee, H. B. Jeon, Y.-K. Choi, K. Yu and S.-Y. Choi, Si–MoS2 vertical heterojunction for a photodetector with high responsivity and low noise equivalent power, *ACS Appl. Mater. Interfaces*, 2019, **11**, 7626–7634.

40 T. Dong, J. Simões and Z. Yang, Flexible photodetector based on 2D materials: processing, architectures, and applications, *Adv. Mater. Interfaces*, 2020, **7**, 1901657.

41 M. Long, P. Wang, H. Fang and W. Hu, Progress, Challenges, and Opportunities for 2D Material Based Photodetectors, *Adv. Funct. Mater.*, 2019, **29**, 1803807.

42 T. Patel and A. W. Tsen, Stress testing the bulk photovoltaic effect, *Nat. Nanotechnol.*, 2023, **18**, 3–4.

43 C. Liu, J. Guo, L. Yu, J. Li, M. Zhang, H. Li, Y. Shi and D. Dai, Silicon/2D-material photodetectors: from near-infrared to mid-infrared, *Light: Sci. Appl.*, 2021, **10**, 123.

44 X. Lu, L. Sun, P. Jiang and X. Bao, Progress of Photodetectors Based on the Photothermoelectric Effect, *Adv. Mater.*, 2019, **31**, 1902044.

45 D. Basko, A photothermoelectric effect in graphene, *Science*, 2011, **334**, 610–611.

46 X. Lu, P. Jiang and X. Bao, Phonon-enhanced photothermoelectric effect in SrTiO3 ultra-broadband photodetector, *Nat. Commun.*, 2019, **10**, 138.

47 T. Case, Notes on the change of resistance of certain substances in light, *Phys. Rev.*, 1917, **9**, 305.

48 M. Casalino, G. Coppola, M. Iodice, I. Rendina and L. Sirleto, Near-infrared sub-bandgap all-silicon photodetectors: state of the art and perspectives, *Sensors*, 2010, **10**, 10571–10600.

49 W. Lei, J. Antoszewski and L. Faraone, Progress, challenges, and opportunities for HgCdTe infrared materials and detectors, *Appl. Phys. Rev.*, 2015, **2**, 041303.

50 H. Yuan, J. Zhang, J. Kim, D. Bond, J. Laquindanum, J. Kimchi and M. G. DeForest, Recent progress in extended wavelength InGaAs photodetectors and comparison with SWIR HgCdTe photodetectors, *Infrared Sensors, Devices, and Applications IX*, 2019, vol. 11129, pp. 97–106.

51 P. Wang, H. Xia, Q. Li, F. Wang, L. Zhang, T. Li, P. Martyniuk, A. Rogalski and W. Hu, Sensing infrared photons at room temperature: from bulk materials to atomic layers, *Small*, 2019, **15**, 1904396.
52 D. Gray, A. McCaughan and B. Mookerji, Crystal structure of graphite, graphene and silicon, *Physics for Solid State Applications*, 2009, **6**, 730.
53 W. Yang, J. Chen, Y. Zhang, Y. Zhang, J. H. He and X. Fang, Silicon-compatible photodetectors: trends to monolithically integrate photosensors with chip technology, *Adv. Funct. Mater.*, 2019, **29**, 1808182.
54 M. A. Green, Intrinsic concentration, effective densities of states, and effective mass in silicon, *J. Appl. Phys.*, 1990, **67**, 2944–2954.
55 M. A. Nazirzadeh, F. B. Atar, B. B. Turgut and A. K. Okyay, Random sized plasmonic nanoantennas on Silicon for low-cost broad-band near-infrared photodetection, *Sci. Rep.*, 2014, **4**, 7103.
56 Y. Cui, Z. Tong, X. Zhang, W. Wang, W. Zhao, Y. Yu, X. Pi, J. Zhang and Z. Ni, Mid-infrared plasmonic silicon quantum dot/HgCdTe photodetector with ultrahigh specific detectivity, *Sci. China Inf. Sci.*, 2023, **66**, 142404.
57 S. Park, J. Jeon, V. M. More, R. S. Lee, Y. Seo, M. Kim, P. D. Nguyen, M. Kim, J. S. Kim and Y. Kim, Monolithic two-color short-wavelength InGaAs infrared photodetectors using InAsP metamorphic buffers, *Appl. Surf. Sci.*, 2022, **581**, 152421.
58 Y. Xie, B. Zhang, S. Wang, D. Wang, A. Wang, Z. Wang, H. Yu, H. Zhang, Y. Chen and M. Zhao, Ultrabroadband MoS2 photodetector with spectral response from 445 to 2717 nm, *Adv. Mater.*, 2017, **29**, 1605972.
59 S. Huang, J. Cao, G. Song, J. Cao, Y. Lu, Q. Wu, W. Gao and J. Xu, Broadband-Spectral-Responsivity of black silicon photodetector with high gain and sub-bandgap sensitivity by titanium hyperdoping, *Opt Laser. Technol.*, 2024, **171**, 110399.
60 A. Rogalski, HgCdTe infrared detector material: history, status and outlook, *Rep. Prog. Phys.*, 2005, **68**, 2267.
61 I. B. Bhat, H. Ehsani and S. K. Ghandhi, The growth and characterization of HgTe and HgCdTe using methylalylltelluride, *J. Vac. Sci. Technol., A*, 1990, **8**, 1054–1058.
62 X. Wang, M. Wang, Y. Liao, H. Zhang, B. Zhang, T. Wen, J. Yi and L. Qiao, Molecular-beam epitaxy-grown HgCdTe infrared detector: Material physics, structure design, and device fabrication, *Sci. China: Phys., Mech. Astron.*, 2023, **66**, 237302.
63 J. Schmit, Growth, properties and applications of HgCdTe, *J. Cryst. Growth*, 1983, **65**, 249–261.
64 Y. Wang, Y. Gu, A. Cui, Q. Li, T. He, K. Zhang, Z. Wang, Z. Li, Z. Zhang and P. Wu, Fast uncooled mid-wavelength infrared photodetectors with heterostructures of van der Waals on epitaxial HgCdTe, *Adv. Mater.*, 2022, **34**, 2107772.
65 H. Jiao, X. Wang, Y. Chen, S. Guo, S. Wu, C. Song, S. Huang, X. Huang, X. Tai and T. Lin, HgCdTe/black phosphorus van der Waals heterojunction for high-performance polarization-sensitive midwave infrared photodetector, *Sci. Adv.*, 2022, **8**, eabn1811.
66 S. An, H. Park and M. Kim, Recent advances in single crystal narrow band-gap semiconductor nanomembranes and their flexible optoelectronic device applications: Ge, GeSn, InGaAs, and 2D materials, *J. Mater. Chem. C*, 2023, **11**, 2430–2448.
67 W. Lee and C. G. Fonstad, The growth of high mobility InGaAs and InAlAs layers by molecular beam epitaxy, *J. Vac. Sci. Technol., B: Microelectron. Process. Phenom.*, 1986, **4**, 536–538.
68 X. Li, J. Zhang, C. Yue, X. Tang, Z. Gao, Y. Jiang, C. Du, Z. Deng, H. Jia and W. Wang, High performance visible-SWIR flexible photodetector based on large-area InGaAs/InP PIN structure, *Sci. Rep.*, 2022, **12**, 7681.
69 D. Kwak, D. K. Polyushkin and T. Mueller, In-sensor computing using a MoS2 photodetector with programmable spectral responsivity, *Nat. Commun.*, 2023, **14**, 4264.
70 Z. Xu, M. He, Q. Wu, C. Wu, X. Li, B. Liu, M. C. Tang, J. Yao and G. Wei, Ultrafast charge transfer 2D MoS2/organic heterojunction for sensitive photodetector, *Adv. Sci.*, 2023, **10**, 2207743.
71 H. Zhang, Ultrathin Two-Dimensional Nanomaterials, *ACS Nano*, 2015, **9**, 9451–9469.
72 V. Tran, R. Soklaski, Y. Liang and L. Yang, Layer-controlled band gap and anisotropic excitons in few-layer black phosphorus, *Phys. Rev. B: Condens. Matter Mater. Phys.*, 2014, **89**, 235319.
73 D.-S. Tsai, K.-K. Liu, D.-H. Lien, M.-L. Tsai, C.-F. Kang, C.-A. Lin, L.-J. Li and J.-H. He, Few-layer MoS2 with high broadband photogain and fast optical switching for use in harsh environments, *ACS Nano*, 2013, **7**, 3905–3911.
74 Z.-S. Wu, W. Ren, L. Gao, J. Zhao, Z. Chen, B. Liu, D. Tang, B. Yu, C. Jiang and H.-M. Cheng, Synthesis of Graphene Sheets with High Electrical Conductivity and Good Thermal Stability by Hydrogen Arc Discharge Exfoliation, *ACS Nano*, 2009, **3**, 411–417.
75 A. K. Geim and K. S. Novoselov, The rise of graphene, *Nat. Mater.*, 2007, **6**, 183–191.
76 F. H. L. Koppens, T. Mueller, P. Avouris, A. C. Ferrari, M. S. Vitiello and M. Polini, Photodetectors based on graphene, other two-dimensional materials and hybrid systems, *Nat. Nanotechnol.*, 2014, **9**, 780–793.
77 G. Konstantatos, M. Badioli, L. Gaudreau, J. Osmond, M. Bernechea, F. Pelayo Garcia de Arquer, F. Gatti and F. H. L. Koppens, Hybrid graphene–quantum dot phototransistors with ultrahigh gain, *Nat. Nanotechnol.*, 2021, **7**, 363–368.
78 J. Park, Y. Ahn and C. Ruiz-Vargas, Imaging of photocurrent generation and collection in single-layer graphene, *Nano Lett.*, 2009, **9**, 1742–1746.
79 F. Xia, T. Mueller, R. Golizadeh-Mojarad, M. Freitag, Y.-m. Lin, J. Tsang, V. Perebeinos and P. Avouris, Photocurrent imaging and efficient photon detection in a graphene transistor, *Nano Lett.*, 2009, **9**, 1039–1044.

80 C.-H. Liu, Y.-C. Chang, T. B. Norris and Z. Zhong, Graphene photodetectors with ultra-broadband and high responsivity at room temperature, *Nat. Nanotechnol.*, 2014, **9**, 273–278.
81 D. Zahn, P.-N. Hildebrandt, T. Vasileiadis, Y. W. Windsor, Y. Qi, H. L. N. Seiler and R. Ernstorfer, Anisotropic nonequilibrium lattice dynamics of black phosphorus, *Nano Lett.*, 2020, **20**, 3728–3733.
82 M. Buscema, D. J. Groenendijk, S. I. Blanter, G. A. Steele, H. S. van der Zant and A. Castellanos-Gomez, Fast and broadband photoresponse of few-layer black phosphorus field-effect transistors, *Nano Lett.*, 2014, **14**, 3347–3352.
83 R. Gusmao, Z. Sofer and M. Pumera, Black phosphorus rediscovered: from bulk material to monolayers, *Angew. Chem., Int. Ed.*, 2017, **56**, 8052–8072.
84 Z. Hu, T. Niu, R. Guo, J. Zhang, M. Lai, J. He, L. Wang and W. Chen, Two-dimensional black phosphorus: its fabrication, functionalization and applications, *Nanoscale*, 2018, **10**, 21575–21603.
85 Q. Guo, A. Pospischil, M. Bhuiyan, H. Jiang, H. Tian, D. Farmer, B. Deng, C. Li, S.-J. Han and H. Wang, Black phosphorus mid-infrared photodetectors with high gain, *Nano Lett.*, 2016, **16**, 4648–4655.
86 D. Kong, H. Wang, J. J. Cha, M. Pasta, K. J. Koski, J. Yao and Y. Cui, Synthesis of MoS2 and MoSe2 films with vertically aligned layers, *Nano Lett.*, 2013, **13**, 1341–1347.
87 H. Wang, C. Li, P. Fang, Z. Zhang and J. Z. Zhang, Synthesis, properties, and optoelectronic applications of two-dimensional MoS 2 and MoS 2-based heterostructures, *Chem. Soc. Rev.*, 2018, **47**, 6101–6127.
88 B. Cao, Z. Ye, L. Yang, L. Gou and Z. Wang, Recent progress in van der Waals 2D PtSe2, *Nanotechnology*, 2021, **32**, 412001.
89 S. Liu and Z. Liu, Hybridization induced metallic and magnetic edge states in noble transition-metal-dichalcogenides of PtX 2 (X= S, Se) nanoribbons, *Phys. Chem. Chem. Phys.*, 2018, **20**, 21441–21446.
90 H. Zhang, H. Li, F. Wang, X. Song, Z. Xu, D. Wei, J. Zhang, Z. Dai, Y. Ren and Y. Ye, PtSe2 field-effect phototransistor with positive and negative photoconductivity, *ACS Appl. Electron. Mater.*, 2022, **4**, 5177–5183.
91 P. Ye, H. Xiao, Q. Zhu, Y. Kong, Y. Tang and M. Xu, Si-CMOS-compatible 2D PtSe2-based self-driven photodetector with ultrahigh responsivity and specific detectivity, *Sci. China Mater.*, 2023, **66**, 193–201.
92 J. Deng, W. Zhang, X. Dai, Y. Yu, Z. Li, W. Wang, L. Wang, J. Zhou and X. Chen, Nonmonotonic wavelength dependence of the polarization-sensitive infrared photoresponse of an anisotropic semimetal, *Nanoscale*, 2022, **14**, 7314–7321.
93 Y. Yi, C. Wu, H. Wang, H. Liu, H. Li, H. Zhang, H. He and J. Wang, Thickness dependent magneto transport properties of WTe2 thin films, *Solid State Commun.*, 2017, **260**, 45–49.
94 Y. Xiao, K. Luo, Q. Kao, Y. Fu, W. Jiang and L. Cao, Photoelectric properties of large area WTe2 thin films prepared by pulsed laser deposition, *Surf. Interfaces*, 2024, **44**, 103670.
95 F. Wang, Y. Zhang, Y. Gao, P. Luo, J. Su, W. Han, K. Liu, H. Li and T. Zhai, 2D metal chalcogenides for IR photodetection, *Small*, 2019, **15**, 1901347.
96 S. Sorifi, M. Moun, S. Kaushik and R. Singh, High-temperature performance of a GaSe nanosheet-based broadband photodetector, *ACS Appl. Electron. Mater.*, 2020, **2**, 670–676.
97 Z. Li, H. Qiao, Z. Guo, X. Ren, Z. Huang, X. Qi, S. C. Dhanabalan, J. S. Ponraj, D. Zhang and J. Li, High-performance photo-electrochemical photodetector based on liquid-exfoliated few-layered InSe nanosheets with enhanced stability, *Adv. Funct. Mater.*, 2018, **28**, 1705237.
98 W. Gao, S. Zhang, F. Zhang, P. Wen, L. Zhang, Y. Sun, H. Chen, Z. Zheng, M. Yang and D. Luo, 2D WS2 based asymmetric Schottky photodetector with high performance, *Adv. Electron. Mater.*, 2021, **7**, 2000964.
99 F. Yan, L. Zhao, A. Patanè, P. Hu, X. Wei, W. Luo, D. Zhang, Q. Lv, Q. Feng and C. Shen, Fast, multicolor photodetection with graphene-contacted p-GaSe/n-InSe van der Waals heterostructures, *Nanotechnology*, 2017, **28**, 27LT01.
100 Q. Lv, F. Yan, X. Wei and K. Wang, High-performance, self-driven photodetector based on graphene sandwiched GaSe/WS2 heterojunction, *Adv. Opt. Mater.*, 2018, **6**, 1700490.
101 W. Zhu, X. Wei, F. Yan, Q. Lv, C. Hu and K. Wang, Broadband polarized photodetector based on p-BP/n-ReS2 heterojunction, *J. Semicond.*, 2019, **40**, 092001.
102 I. Tantis, S. Talande, V. Tzitzios, G. Basina, V. Shrivastav, A. Bakandritsos and R. Zboril, Non-van der Waals 2D Materials for Electrochemical Energy Storage, *Adv. Funct. Mater.*, 2023, **33**, 2209360.
103 H. Chen, J. N. B. Rodrigues, A. J. E. Rettie, T.-B. Song, D. G. Chica, X. Su, J.-K. Bao, D. Y. Chung, W.-K. Kwok, L. K. Wagner and M. G. Kanatzidis, High Hole Mobility and Nonsaturating Giant Magnetoresistance in the New 2D Metal NaCu4Se4 Synthesized by a Unique Pathway, *J. Am. Chem. Soc.*, 2019, **141**, 635–642.
104 J.-K. Bao, C. D. Malliakas, C. Zhang, S. Cai, H. Chen, A. J. E. Rettie, B. L. Fisher, D. Y. Chung, V. P. Dravid and M. G. Kanatzidis, Quasi-Two-Dimensional Heterostructures (KM1 – xTe)(LaTe3) (M = Mn and Zn) with Charge Density Waves, *Chem. Mater.*, 2021, **33**, 2155–2164.
105 H. Chen, J. He, C. D. Malliakas, C. C. Stoumpos, A. J. E. Rettie, J.-K. Bao, D. Y. Chung, W.-K. Kwok, C. Wolverton and M. G. Kanatzidis, A Natural 2D Heterostructure [Pb3.1Sb0.9S4][AuxTe2–x] with Large Transverse Nonsaturating Negative Magnetoresistance and High Electron Mobility, *J. Am. Chem. Soc.*, 2019, **141**, 7544–7553.
106 M. P. Smylie, K. Willa, J. K. Bao, K. Ryan, Z. Islam, H. Claus, Y. Simsek, Z. Diao, A. Rydh, A. E. Koshelev, W. K. Kwok, D. Y. Chung, M. G. Kanatzidis and U. Welp, Anisotropic superconductivity and magnetism in single-crystals $RbEuFe_4As_4$, *Phys. Rev. B*, 2018, **98**, 104503.

107 Q. Wei, R. Li, C. Lin, A. Han, A. Nie, Y. Li, L.-J. Li, Y. Cheng and W. Huang, Quasi-Two-Dimensional Se-Terminated Bismuth Oxychalcogenide (Bi2O2Se), *ACS Nano*, 2019, **13**, 13439–13444.

108 Y. Y. Niu, D. Wu, L. Shen and B. Wang, A layered antiferromagnetic semiconductor EuMTe3 (M = Bi, Sb), *Phys. Status Solidi RRL*, 2015, **9**, 735–739.

109 H. Xu, A. Ren, J. Wu and Z. Wang, Recent Advances in 2D MXenes for Photodetection, *Adv. Funct. Mater.*, 2020, **30**, 2000907.

110 J. Wu, H. Yuan, M. Meng, C. Chen, Y. Sun, Z. Chen, W. Dang, C. Tan, Y. Liu, J. Yin, Y. Zhou, S. Huang, H. Q. Xu, Y. Cui, H. Y. Hwang, Z. Liu, Y. Chen, B. Yan and H. Peng, High electron mobility and quantum oscillations in non-encapsulated ultrathin semiconducting Bi2O2Se, *Nat. Nanotechnol.*, 2017, **12**, 530–534.

111 T. Tu, Y. Zhang, T. Li, J. Yu, L. Liu, J. Wu, C. Tan, J. Tang, Y. Liang, C. Zhang, Y. Dai, Y. Han, K. Lai and H. Peng, Uniform High-k Amorphous Native Oxide Synthesized by Oxygen Plasma for Top-Gated Transistors, *Nano Lett.*, 2020, **20**, 7469–7475.

112 X. Ma, D. Chang, C. Zhao, R. Li, X. Huang, Z. Zeng, X. Huang and Y. Jia, Geometric structures and electronic properties of the Bi2X2Y (X, Y = O, S, Se, and Te) ternary compound family: a systematic DFT study, *J. Mater. Chem. C*, 2018, **6**, 13241–13249.

113 Y.-D. Xu, C. Wang, Y.-Y. Lv, Y. B. Chen, S.-H. Yao and J. Zhou, Infrared and Raman spectra of Bi2O2X and Bi2OX2 (X = S, Se, and Te) studied from first principles calculations, *RSC Adv.*, 2019, **9**, 18042–18049.

114 H. Kim and H. N. Alshareef, MXetronics: MXene-enabled electronic and photonic devices, *ACS Mater. Lett.*, 2019, **2**, 55–70.

115 Z. Guo, Z. Xu, S. Teo, C. Zhang, Y. Kamata, S. Hayase, T. Ma and L. Gao, High Electrical Conductivity 2D MXene Serves as Additive of Perovskite for Efficient Solar Cells, *Small*, 2018, **14**, 1802738.

116 N. M. Abbasi, Y. Xiao, L. Peng, Y. Duo, L. Wang, L. Zhang, B. Wang and H. Zhang, Recent advancement for the synthesis of MXene derivatives and their sensing protocol, *Adv. Mater. Technol.*, 2021, **6**, 2001197.

117 L. Shen, H. Qian, Y. Yang, Y. Ma, J. Deng and Y. Zhang, Photoresponse Improvement of InGaAs Nanowire Near-Infrared Photodetectors with Self-Assembled Monolayers, *J. Phys. Chem. C*, 2023, **127**, 11328–11337.

118 M.-Q. Li, L.-Y. Dang, G.-G. Wang, F. Li, M. Han, Z.-P. Wu, G.-Z. Li, Z. Liu and J.-C. Han, Bismuth Oxychalcogenide Nanosheet: Facile Synthesis, Characterization, and Photodetector Application, *Adv. Mater. Technol.*, 2020, **5**, 2000180.

119 K. Wang, H. Qiao, J. Li and X. Qi, A robust photoelectrochemical photodetectors based on the self-healing properties of Bi2O2S nanoplates, *Appl. Surf. Sci.*, 2021, **565**, 150444.

120 P. Rong, S. Gao, M. Zhang, S. Ren, H. Lu, J. Jia, S. Jiao, Y. Zhang and J. Wang, Large-area hierarchical Bi2O2S flowers composed of 2D ultrathin nanosheets for high performance self-powered IR photodetector, *J. Alloys Compd.*, 2022, **928**, 167128.

121 J. Yin, Z. Tan, H. Hong, J. Wu, H. Yuan, Y. Liu, C. Chen, C. Tan, F. Yao, T. Li, Y. Chen, Z. Liu, K. Liu and H. Peng, Ultrafast and highly sensitive infrared photodetectors based on two-dimensional oxyselenide crystals, *Nat. Commun.*, 2018, **9**, 3311.

122 Y. Chen, W. Ma, C. Tan, M. Luo, W. Zhou, N. Yao, H. Wang, L. Zhang, T. Xu, T. Tong, Y. Zhou, Y. Xu, C. Yu, C. Shan, H. Peng, F. Yue, P. Wang, Z. Huang and W. Hu, Broadband Bi2O2Se Photodetectors from Infrared to Terahertz, *Adv. Funct. Mater.*, 2021, **31**, 2009554.

123 Y. Wei, C. Chen, C. Tan, L. He, Z. Ren, C. Zhang, S. Peng, J. Han, H. Zhou and J. Wang, High-Performance Visible to Near-Infrared Broadband Bi2O2Se Nanoribbon Photodetectors, *Adv. Opt. Mater.*, 2022, **10**, 2201396.

124 X. Zou, R. Wang, Y. Sun and C. Wang, Two-dimensional Bi2O2Se nanosheets for sensitive and fast-response high-temperature photodetectors, *J. Materiomics*, 2023, **9**, 1024–1031.

125 C. Hu, Z. Du, Z. Wei, L. Li and G. Shen, Functionalized Ti3C2Tx MXene with layer-dependent band gap for flexible NIR photodetectors, *Appl. Phys. Rev.*, 2023, **10**, 021402.

126 C. Hu, Z. Wei, L. Li and G. Shen, Strategy Toward Semiconducting Ti3C2Tx-MXene: Phenylsulfonic Acid Groups Modified Ti3C2Tx as Photosensitive Material for Flexible Visual Sensory-Neuromorphic System, *Adv. Funct. Mater.*, 2023, **33**, 2302188.

127 W. Yu, S. Li, Y. Zhang, W. Ma, T. Sun, J. Yuan, K. Fu and Q. Bao, Near-infrared photodetectors based on MoTe2/graphene heterostructure with high responsivity and flexibility, *Small*, 2017, **13**, 1700268.

128 F. Luo, M. Zhu, H. Sun, W. Luo, G. Peng, Z. Zhu, X.-A. Zhang and S. Qin, High responsivity graphene photodetectors from visible to near-infrared by photogating effect, *AIP Adv.*, 2018, **8**, 115106.

129 S. N. S. Yadav, P. L. Chen, C. H. Liu and T. J. Yen, Plasmonic Metasurface Integrated Black Phosphorus-Based Mid-Infrared Photodetector with High Responsivity and Speed, *Adv. Mater. Interfaces*, 2023, **10**, 2202403.

130 C. Wang, Q. Wu, Y. Ding, X. Zhang, W. Wang, X. Guo, Z. Ni, L. Lin, Z. Cai and X. Gu, High-responsivity and broadband MoS2 photodetector using interfacial engineering, *ACS Appl. Mater. Interfaces*, 2023, **15**, 46236–46246.

131 C. Hu, Z. Wei, L. Li and G. Shen, Strategy Toward Semiconducting Ti3C2Tx-MXene: Phenylsulfonic Acid Groups Modified Ti3C2Tx as Photosensitive Material for Flexible Visual Sensory-Neuromorphic System, *Adv. Funct. Mater.*, 2023, **33**, 2302188.

132 S. D. N. Luu and P. Vaqueiro, Synthesis, characterisation and thermoelectric properties of the oxytelluride Bi2O2Te, *J. Solid State Chem.*, 2015, **226**, 219–223.

133 Q. Lin, Z. Yu, L. Lu, X. Huang, Q. Wei and D. Tang, Smartphone-based photoelectrochemical immunoassay of

prostate-specific antigen based on Co-doped Bi2O2S nanosheets, *Biosens. Bioelectron.*, 2023, **230**, 115260.

134 C. Huang, H. Yu, J. Chen, J. Zhang, Z. Wu and C. Hou, Improved performance of polymer solar cells by doping with Bi2O2S nanocrystals, *Sol. Energy Mater. Sol. Cells*, 2019, **200**, 110030.

135 X. Zou, H. Liang, Y. Li, Y. Zou, F. Tian, Y. Sun and C. Wang, 2D Bi2O2Te Semiconductor with Single-Crystal Native Oxide Layer, *Adv. Funct. Mater.*, 2023, **33**, 2213807.

136 X. Zhang, Y. Liu, G. Zhang, Y. Wang, H. Zhang and F. Huang, Thermal Decomposition of Bismuth Oxysulfide from Photoelectric Bi2O2S to Superconducting Bi4O4S3, *ACS Appl. Mater. Interfaces*, 2015, **7**, 4442–4448.

137 M. Wu and X. C. Zeng, Bismuth Oxychalcogenides: A New Class of Ferroelectric/Ferroelastic Materials with Ultra High Mobility, *Nano Lett.*, 2017, **17**, 6309–6314.

138 T. Ghosh, M. Samanta, A. Vasdev, K. Dolui, J. Ghatak, T. Das, G. Sheet and K. Biswas, Ultrathin Free-Standing Nanosheets of Bi2O2Se: Room Temperature Ferroelectricity in Self-Assembled Charged Layered Heterostructure, *Nano Lett.*, 2019, **19**, 5703–5709.

139 W. Wang, Y. Meng, Y. Zhang, Z. Zhang, W. Wang, Z. Lai, P. Xie, D. Li, D. Chen, Q. Quan, D. Yin, C. Liu, Z. Yang, S. Yip and J. C. Ho, Electrically Switchable Polarization in Bi2O2Se Ferroelectric Semiconductors, *Adv. Mater.*, 2023, **35**, 2210854.

140 F. Wang, S. Yang, J. Wu, X. Hu, Y. Li, H. Li, X. Liu, J. Luo and T. Zhai, Emerging two-dimensional bismuth oxychalcogenides for electronics and optoelectronics, *InfoMat*, 2021, **3**, 1251–1271.

141 J. Dong, L. Zhang, K. Lau, Y. Shu, S. Wang, Z. Fu, Z. Wu, X. Liu, B. Sa, J. Pei, J. Zheng, H. Zhan and Q. Wang, Tailoring Broadband Nonlinear Optical Characteristics and Ultrafast Photocarrier Dynamics of Bi2O2S Nanosheets by Defect Engineering, *Small*, 2024, **20**, 2309595.

142 L. Xu, S. Liu, H. Zhang, X. Zhang, J. Li, J. Yan, B. Shi, J. Yang, C. Yang, L. Xu, X. Sun and J. Lu, First-principles simulation of monolayer hydrogen passivated Bi2O2S2–metal interfaces, *Phys. Chem. Chem. Phys.*, 2020, **22**, 7853–7863.

143 Y. Sun, J. Zhang, S. Ye, J. Song and J. Qu, Progress Report on Property, Preparation, and Application of Bi2O2Se, *Adv. Funct. Mater.*, 2020, **30**, 2004480.

144 S. Liu, C. Tan, D. He, Y. Wang, H. Peng and H. Zhao, Optical Properties and Photocarrier Dynamics of Bi2O2Se Monolayer and Nanoplates, *Adv. Opt. Mater.*, 2020, **8**, 1901567.

145 C. Chen, M. Wang, J. Wu, H. Fu, H. Yang, Z. Tian, T. Tu, H. Peng, Y. Sun, X. Xu, J. Jiang, N. B. M. Schröter, Y. Li, D. Pei, S. Liu, S. A. Ekahana, H. Yuan, J. Xue, G. Li, J. Jia, Z. Liu, B. Yan, H. Peng and Y. Chen, Electronic structures and unusually robust bandgap in an ultrahigh-mobility layered oxide semiconductor, Bi2O2Se, *Sci. Adv.*, 2018, **4**, eaat8355.

146 T. Tong, M. Zhang, Y. Chen, Y. Li, L. Chen, J. Zhang, F. Song, X. Wang, W. Zou, Y. Xu and R. Zhang, Ultrahigh Hall mobility and suppressed backward scattering in layered semiconductor Bi2O2Se, *Appl. Phys. Lett.*, 2018, **113**, 072106.

147 G. Wang, F. Liu, R. Chen, M. Wang, Y. Yin, J. Zhang, Z. Sa, P. Li, J. Wan, L. Sun, Z. Lv, Y. Tan, F. Chen and Z.-x. Yang, Tunable Contacts of Bi2O2Se Nanosheets MSM Photodetectors by Metal-Assisted Transfer Approach for Self-Powered Near-Infrared Photodetection, *Small*, 2024, **20**, 2306363.

148 Z. Zhang, L. Han, Z. Dan, H. Li, M. Yang, Y. Sun, Z. Zheng, N. Huo, D. Luo, W. Gao and J. Li, Type II Homo-Type Bi2O2Se Nanosheet/InSe Nanoflake Heterostructures for Self-Driven Broadband Visible–Near-Infrared Photodetectors, *ACS Appl. Nano Mater.*, 2023, **6**, 4573–4583.

149 L. Zhang, Y. He, X. Dong, J. Guo, Z. Gao, Z. Liu, J. Chen, Y. Zhao, Z. Zhou, J. Yin, X. Fu, F. Luo, H. Fu and J. Wu, Controlled Synthesis of a High-Mobility Bi3O2.5Se2 Semiconductor by Oxidation of Bi2Se3 for Fast and Highly Sensitive Photodetectors, *Laser Photonics Rev.*, 2024, **18**, 2300854.

150 P. Luo, F. Wang, J. Qu, K. Liu, X. Hu, K. Liu and T. Zhai, Self-Driven WSe2/Bi2O2Se Van der Waals Heterostructure Photodetectors with High Light On/Off Ratio and Fast Response, *Adv. Funct. Mater.*, 2021, **31**, 2008351.

151 J. Li, Z. Wang, Y. Wen, J. Chu, L. Yin, R. Cheng, L. Lei, P. He, C. Jiang, L. Feng and J. He, High-Performance Near-Infrared Photodetector Based on Ultrathin Bi2O2Se Nanosheets, *Adv. Funct. Mater.*, 2018, **28**, 1706437.

152 P. Luo, F. Zhuge, F. Wang, L. Lian, K. Liu, J. Zhang and T. Zhai, PbSe Quantum Dots Sensitized High-Mobility Bi2O2Se Nanosheets for High-Performance and Broadband Photodetection Beyond 2 μm, *ACS Nano*, 2019, **13**, 9028–9037.

153 C. Tan, S. Xu, Z. Tan, L. Sun, J. Wu, T. Li and H. Peng, Exploitation of Bi2O2Se/graphene van der Waals heterojunction for creating efficient photodetectors and short-channel field-effect transistors, *InfoMat*, 2019, **1**, 390–395.

154 S. Yang, S. Jiao, Y. Nie, Y. Zhao, S. Gao, D. Wang and J. Wang, A high-performance and self-powered polarization-sensitive photoelectrochemical-type Bi2O2Te photodetector based on a quasi-solid-state gel electrolyte, *Mater. Horiz.*, 2024, **11**, 1710–1718.

155 Z. Hui, X. Bu, Y. Wang, D. Han, J. Gong, L. Li, X. Li and S. Yan, Bi2O2Te Nanosheets Saturable Absorber-Based Passive Mode-Locked Fiber Laser: From Soliton Molecules to Harmonic Soliton, *Adv. Opt. Mater.*, 2022, **10**, 2201812.

156 J.-X. Chen, X.-G. Zhao, X.-X. Dong, Z.-L. Lv and H.-L. Cui, Density Functional Study of the Electronic, Elastic and Optical Properties of Bi2O2Te, *Z. Naturforsch. A*, 2020, **75**, 73–80.

157 W. Ai, J. Chen, X. Dong, Z. Gao, Y. He, Z. Liu, H. Fu, F. Luo and J. Wu, High Mobility and Quantum Oscillations in Semiconducting Bi2O2Te Nanosheets Grown by Chemical Vapor Deposition, *Nano Lett.*, 2022, **22**, 7659–7666.

158 M. Han, D. Zhang, C. E. Shuck, B. McBride, T. Zhang, R. Wang, K. Shevchuk and Y. Gogotsi, Electrochemically

modulated interaction of MXenes with microwaves, *Nat. Nanotechnol.*, 2023, **18**, 373–379.
159 C. Zhang and V. Nicolosi, Graphene and MXene-based transparent conductive electrodes and supercapacitors, *Energy Storage Mater.*, 2019, **16**, 102–125.
160 C. Zhang, B. Anasori, A. Seral-Ascaso, S.-H. Park, N. McEvoy, A. Shmeliov, G. S. Duesberg, J. N. Coleman, Y. Gogotsi and V. Nicolosi, Transparent, Flexible, and Conductive 2D Titanium Carbide (MXene) Films with High Volumetric Capacitance, *Adv. Mater.*, 2017, **29**, 1702678.
161 K. Hantanasirisakul, M.-Q. Zhao, P. Urbankowski, J. Halim, B. Anasori, S. Kota, C. E. Ren, M. W. Barsoum and Y. Gogotsi, Fabrication of Ti3C2Tx MXene Transparent Thin Films with Tunable Optoelectronic Properties, *Adv. Electron. Mater.*, 2016, **2**, 1600050.
162 B. Aïssa, A. Ali, K. A. Mahmoud, T. Haddad and M. Nedil, Transport properties of a highly conductive 2D Ti3C2Tx MXene/graphene composite, *Appl. Phys. Lett.*, 2016, **109**, 043109.
163 K. Montazeri, M. Currie, L. Verger, P. Dianat, M. W. Barsoum and B. Nabet, Beyond Gold: Spin-Coated Ti3C2-Based MXene Photodetectors, *Adv. Mater.*, 2019, **31**, 1903271.
164 K. Montazeri, M. Currie, M. W. Barsoum and B. Nabet, Ultra-High Speed, High-Sensitivity Spin-Cast MXene-Semiconductor-MXene Photodetectors, *Adv. Funct. Mater.*, 2022, **32**, 2206942.
165 W. Song, Q. Liu, J. Chen, Z. Chen, X. He, Q. Zeng, S. Li, L. He, Z. Chen and X. Fang, Interface Engineering Ti3C2 MXene/Silicon Self-Powered Photodetectors with High Responsivity and Detectivity for Weak Light Applications, *Small*, 2021, **17**, 2100439.
166 L. Luo, Y. Huang, K. Cheng, A. Alhassan, M. Alqahtani, L. Tang, Z. Wang and J. Wu, MXene-GaN van der Waals metal-semiconductor junctions for high performance multiple quantum well photodetectors, *Light: Sci. Appl.*, 2021, **10**, 177.
167 L. Gao, Y. Zhao, X. Chang, J. Zhang, Y. Li, S. Wageh, O. A. Al-Hartomy, A. G. Al-Sehemi, H. Zhang and H. Ågren, Emerging applications of MXenes for photodetection: Recent advances and future challenges, *Mater. Today*, 2022, **61**, 169–190.
168 B. Li, Q.-B. Zhu, C. Cui, C. Liu, Z.-H. Wang, S. Feng, Y. Sun, H.-L. Zhu, X. Su, Y.-M. Zhao, H.-W. Zhang, J. Yao, S. Qiu, Q.-W. Li, X.-M. Wang, X.-H. Wang, H.-M. Cheng and D.-M. Sun, Patterning of Wafer-Scale MXene Films for High-Performance Image Sensor Arrays, *Adv. Mater.*, 2022, **34**, 2201298.
169 M. Naguib, M. W. Barsoum and Y. Gogotsi, Ten years of progress in the synthesis and development of MXenes, *Adv. Mater.*, 2021, **33**, 2103393.
170 D. H. Ho, Y. Y. Choi, S. B. Jo, J. M. Myoung and J. H. Cho, Sensing with MXenes: progress and prospects, *Adv. Mater.*, 2021, **33**, 2005846.
171 B. Anasori, M. R. Lukatskaya and Y. Gogotsi, 2D metal carbides and nitrides (MXenes) for energy storage, *Nat. Rev. Mater.*, 2017, **2**, 16098.
172 M. Naguib, M. Kurtoglu, V. Presser, J. Lu, J. Niu, M. Heon, L. Hultman, Y. Gogotsi and M. W. Barsoum, Two-Dimensional Nanocrystals Produced by Exfoliation of Ti3AlC2, *Adv. Mater.*, 2011, **23**, 4248–4253.
173 Y. Di, K. Ba, Y. Chen, X. Wang, M. Zhang, X. Huang, Y. Long, M. Liu, S. Zhang, W. Tang, Z. Huang, T. Lin, H. Shen, X. Meng, M. Han, Q. Liu and J. Wang, Interface Engineering to Drive High-Performance MXene/PbS Quantum Dot NIR Photodiode, *Adv. Sci.*, 2024, **11**, 2307169.
174 A. D. Dillon, M. J. Ghidiu, A. L. Krick, J. Griggs, S. J. May, Y. Gogotsi, M. W. Barsoum and A. T. Fafarman, Highly Conductive Optical Quality Solution-Processed Films of 2D Titanium Carbide, *Adv. Funct. Mater.*, 2016, **26**, 4162–4168.
175 B. Liu, L. Qian, Y. Zhao, Y. Zhang, F. Liu, Y. Zhang, Y. Xie and W. Shi, A polarization-sensitive, self-powered, broadband and fast Ti3C2T x MXene photodetector from visible to near-infrared driven by photogalvanic effects, *Front. Phys.*, 2022, **17**, 53501.
176 M. Yousefi, P. Ghaffari, R. Nosrati, S. Dehghani, A. Salmaninejad, Y. J. Abarghan and S. H. Ghaffari, Prognostic and therapeutic significance of circulating tumor cells in patients with lung cancer, *Cell. Oncol.*, 2020, **43**, 31–49.
177 S. Sun, S. Yang, X. Hu, C. Zheng, H. Song, L. Wang, Z. Shen and Z.-S. Wu, Combination of immunomagnetic separation with aptamer-mediated double rolling circle amplification for highly sensitive circulating tumor cell detection, *ACS Sens.*, 2020, **5**, 3870–3878.
178 P. Gopinathan, N.-J. Chiang, C.-H. Wang, A. Sinha, Y.-C. Tsai, H.-C. Tu, S.-C. Hung, P.-H. Hsu, Y.-S. Shan and G.-B. Lee, Aptamer probed isolation of circulating tumor cells in cholangiocarcinoma patients, *Sens. Actuators, B*, 2020, **322**, 128569.
179 M. Zhang, C. Wang, C. Yang, H. Wu, H. Xu and G. Liang, Using fluorescence on/off to trace tandem nanofiber assembly/disassembly in living cells, *Anal. Chem.*, 2021, **93**, 5665–5669.
180 C. Ding, C. Zhang, X. Yin, X. Cao, M. Cai and Y. Xian, Near-infrared fluorescent Ag2S nanodot-based signal amplification for efficient detection of circulating tumor cells, *Anal. Chem.*, 2018, **90**, 6702–6709.
181 B. Zhang, H. Wang, J. Xi, F. Zhao and B. Zeng, A novel Z-scheme ZnIn2S4/WO3 photocatalyst based photoelectrochemical immunosensor for the sensitive detection of prostate specific antigen, *Sens. Actuators, B*, 2019, **298**, 126835.
182 X. Xu, Z. Ding, X. Zhang, R. Zha, W. Li, L. Xu, D. Sun, X. Cai, T. Liang and Y. Wang, A near-infrared photoelectrochemical aptasensing system based on Bi2O2S nanoflowers and gold nanoparticles for high-performance determination of MCF-7ácells, *Anal. Chim. Acta*, 2023, **1251**, 340982.
183 C. Hu, H. Chen, L. Li, H. Huang and G. Shen, Ti3C2Tx MXene-RAN van der Waals Heterostructure-Based Flexible Transparent NIR Photodetector Array for 1024

Pixel Image Sensing Application, *Adv. Mater. Technol.*, 2022, **7**, 2101639.

184 D. Palanker, Femtosecond lasers for ophthalmic surgery enabled by chirped-pulse amplification, *N. Engl. J. Med.*, 2018, **379**, 2267–2269.

185 Y. Zhu, C. Geng, L. Hu, L. Liu, Y. Zhu, Y. Yao, C. Li, Y. Ma, G. Li and Y. Chen, Skin-Like Near-Infrared II Photodetector with High Performance for Optical Communication, Imaging, and Proximity Sensing, *Chem. Mater.*, 2023, **35**, 2114–2124.

186 J. Gjerde and R. A. Jishi, Hyperbolic Behavior and Antiferromagnetic Order in Rare-Earth Tellurides, *Crystals*, 2022, **12**, 1839.

187 K. Yumigeta, Y. Qin, H. Li, M. Blei, Y. Attarde, C. Kopas and S. Tongay, Advances in Rare-Earth Tritelluride Quantum Materials: Structure, Properties, and Synthesis, *Adv. Sci.*, 2021, **8**, 2004762.

188 A. M. Tokmachev, D. V. Averyanov, A. N. Taldenkov, O. E. Parfenov, I. A. Karateev, I. S. Sokolov and V. G. Storchak, Lanthanide f7 metalloxenes – a class of intrinsic 2D ferromagnets, *Mater. Horiz.*, 2019, **6**, 1488–1496.

189 S. Lei, J. Lin, Y. Jia, M. Gray, A. Topp, G. Farahi, S. Klemenz, T. Gao, F. Rodolakis, J. L. McChesney, C. R. Ast, A. Yazdani, K. S. Burch, S. Wu, N. P. Ong and L. M. Schoop, High mobility in a van der Waals layered antiferromagnetic metal, *Sci. Adv.*, 2020, **6**, eaay6407.

190 Z. Gao, Y. Wang, J. Gao, Z. Cui, X. Zhang, J. Shi and X. Fan, Bipolar ferromagnetic semiconductor with large magnetic moment: EuGe2 monolayer, *Comput. Mater. Sci.*, 2022, **213**, 111611.

191 O. E. Parfenov, D. V. Averyanov, A. M. Tokmachev, I. S. Sokolov, I. A. Karateev, A. N. Taldenkov and V. G. Storchak, High-Mobility Carriers in Germanene Derivatives, *Adv. Funct. Mater.*, 2020, **30**, 1910643.

192 G. Yang, J.-S. Chai, K. Bu, L.-F. Xu and J.-T. Wang, Structural, magnetic, and electronic properties of EuSi2 thin films on the Si(111) surface, *Phys. Chem. Chem. Phys.*, 2022, **24**, 6782–6787.

193 Y. Wang, Z. Cui, H. Zeng, Z. Wang, X. Zhang, J. Shi, T. Cao and X. Fan, Tunable magnetic order in two-dimensional layered GdGe2, *J. Mater. Chem. C*, 2022, **10**, 1259–1269.